MICROCOPY RESOLUTION TEST CHART
NATIONAL BUREAU OF STANDARDS-1963-A

AFOSR-TR 85-0

AD-A161 099

CLUSTERING AND ORDERING IN III-V ALLOYS

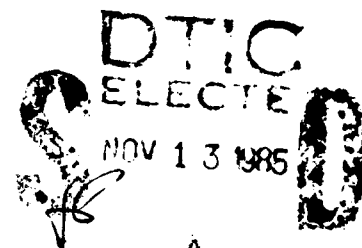SEMICONDUCTOR RESEARCH LABORATORY

Washington University

Saint Louis, Missouri 63130

31 July 1985

DTIC
ELECTE
NOV 1 3 1985

1 June 1984 to 31 May 1985

ANNUAL SCIENTIFIC REPORT NO. WU/SRL-59583A-9

DTIC FILE COPY

85 11 12 138

REPORT DOCUMENTATION PAGE		READ INSTRUCTIONS BEFORE COMPLETING FORM
1. REPORT NUMBER **AFOSR·TR· 8 5 - 0 9 3 1**	2. GOVT ACCESSION NO. *AD-A161 099*	3. RECIPIENT'S CATALOG NUMBER
4. TITLE *(and Subtitle)* Clustering and Ordering in III-V Alloys		5. TYPE OF REPORT & PERIOD COVERED Annual 1 June 84-31 May 85
		6. PERFORMING ORG. REPORT NUMBER WU/SRL 59583A-9
7. AUTHOR(s) C.M. Wolfe, M.W. Muller, S. Julie Hsieh, Elizabeth A. Patten, P. Reblin, R.A. Salzman		8. CONTRACT OR GRANT NUMBER(s) AFOSR-82-0231
9. PERFORMING ORGANIZATION NAME AND ADDRESS Washington University Box 1127 St. Louis, MO 63130		10. PROGRAM ELEMENT, PROJECT, TASK AREA & WORK UNIT NUMBERS 2306/B1 *PE. 61102F*
11. CONTROLLING OFFICE NAME AND ADDRESS Air Force Office of Scientific Researh Building 410 Bolling AFB, DC 20332		12. REPORT DATE 31 July 85
		13. NUMBER OF PAGES 133
14. MONITORING AGENCY NAME & ADDRESS(*if different from Controlling Office*)		15. SECURITY CLASS. *(of this report)* Unclassified
		15a. DECLASSIFICATION. DOWNGRADING SCHEDULE

16. DISTRIBUTION STATEMENT *(of this Report)*

The United States Government is authorized to reproduce and distribute this report for Governmental purposes.

Approved for public release; distribution unlimited.

17. DISTRIBUTION STATEMENT *(of the abstract entered in Block 20, if different from Report)*

18. SUPPLEMENTARY NOTES

19. KEY WORDS *(Continue on reverse side if necessary and identify by block number)*

$ZnSnP_2$, $In_xGa_{1-x}P$, $Al_xGa_{1-x}As$, GaAs, heterojunctions, interfacial energy gaps, generalized Wannier functions, alloy formation, long-range ordering, primitive layered structure.

20. ABSTRACT *(Continue on reverse side if necessary and identify by block number)*

Staggered lineup heterojunctions are expected to exhibit tunneling assisted optical transitions across the interfacial energy gap E_I. In the staggered lineup, E_I is smaller than either of the energy gaps of the constituent semiconductors. In this work, we examined two staggered lineup heterojunctions, $ZnSnP_2$/GaAs and $In_{1-x}Ga_xP$ GaAs. Below bandgap emission and absorption were observed in these structures, allowing the experimental determination

DD FORM 1473 EDITION OF 1 NOV 65 IS OBSOLETE

20. Abstract (Continued)

of E_I. Good agreement was seen between this value of E_I and that from the predicted band lineup.

Advances in technology have made possible the fabrication of rapidly varying heterostructures which hold the promise of important applications. We develop a set of approximate treatments of electron states in a variety of layered heterostructures, The approximations are all based on the concept of one-band generalized Wannier functions. Following a discussion of the validity of this representation, we apply it to an evaluation of the bound states in a narrow quantum well in GaAs, which clearly demonstrates the mixing of main and satellite valley states as well as the contribution of evanescent states. We also evaluate the states of a super-lattice in a model structure of up to 20 quantum wells. As a final example we discuss the application of generalized Wannier functions to the matching of electronic states at a heterojunction between two model band structures with different effective masses, and compare the formalism with alternative approaches to this problem.

Recent III-V alloy formation models indicate that negative charge transfer energy can overcome positive bond distortion energy to stabilize long-range order or compound formation. Although a report of a layered ordering in $Al_xGa_{1-x}As$ tends to confirm this result, we have as yet obtained no convincing evidence for such ordering in $In_xGa_{1-x}P$. Compound formation in these alloys may be critically dependent on growth temperature and kinetic factors.

TABLE OF CONTENTS

1. INTRODUCTION

Although there is substantial interest in III-V semiconductor alloys for electronic and optoelectronic devices, relatively little is known about the distribution of atoms in these materials or the effects of non-random distributions on device performance. In many of these alloys, however, non-random distributions of atoms are expected to be important from thermodynamic considerations. This is particularly true at the low temperatures commonly used for epitaxial growth. The available evidence suggests that short-range clustering of like atoms or short-range ordering of unlike atoms can produce device problems such as excess noise and leakage current, premature voltage breakdown, and lower carrier mobilities. Long-range ordering of unlike atoms, however, could potentially yield III-V ternary compounds with properties superior to their parent alloys. In epitaxial growth, substrate effects such as lattice match and non-equivalent sublattice sites are expected to have a strong influence on these phenomena. Also, two of the important III-V alloys, $Ga_xIn_{1-x}P$ and $Ga_xIn_{1-x}As$, can be epitaxially grown matched to GaAs and InP, respectively, at compositions near the point of greatest ordering probability. The objective of this work is to investigate various aspects of clustering and ordering in III-V alloys, including the interfacial properties of the materials.

2. STAGGERED LINEUP HETEROJUNCTIONS

There are three flat band heterojunction lineups with non-zero band offsets. These flat band lineups are shown in Figure 1, where the three types of lineup, the straddling, the staggered, and the broken-gap lineups are named according to terminology from a previous publication [1]. The lineups shown are called flat band lineups to indicate there is no band bending resulting from deviations from local charge neutrality. Band bending in the equilibrium and forward-biased lineups will be considered later. The straddling lineup, which is the most common, results when the valence band maximum of the larger bandgap material lies below that of the smaller bandgap material. The less common staggered lineup has both band edges of one material below the respective band edges of the other material. The fairly rare broken-gap lineup is that having the conduction band minimum of one semiconductor below the valence band maxima of the other.

The band lineup we will be concerned with in this work is the staggered lineup. The reason this lineup is so interesting is because of the energy gap that exists between the lower conduction band edge and the higher valence band edge at the hetero-interface. This interfacial energy gap, E_I, as seen in the middle of
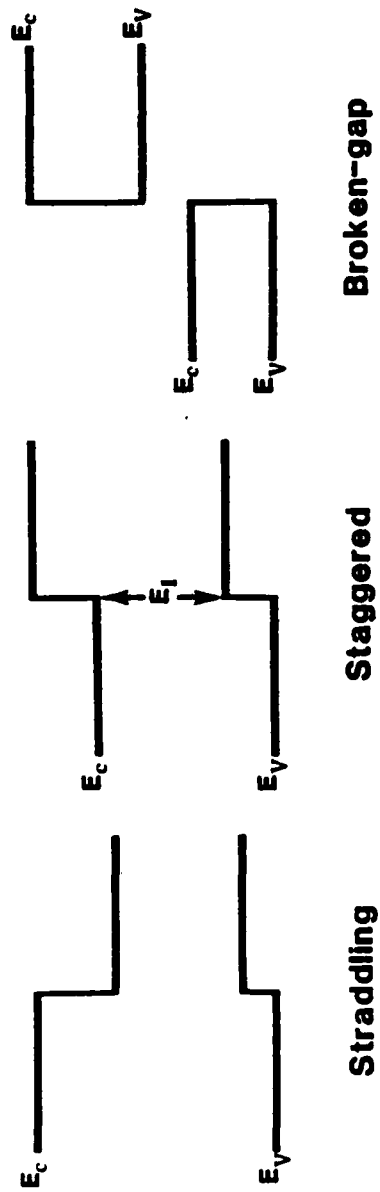
Figure 1   Heterojunction flat band lineups.

Figure 1, is smaller than the bandgaps of either of the constituent semiconductors. This is the essential feature of the staggered lineup heterojunction that has led to discussions of this lineup being a potential source of below bandgap emission and absorption [2,3].

Several different lattice-matched materials systems have been studied to determine the viability of the staggered lineup heterojunction as a below bandgap emitter or detector. E.J. Caine and co-workers have investigated $p-Al_{0.48}In_{0.52}As/n-InP$ grown by molecular beam epitaxy (MBE) [4]. They observed below bandgap electroluminescence at 1.4K which peaked at 0.97eV for a pulsed current density of 4.5 A/cm^2. They used this peak energy value as roughly equal to E_I, and found reasonable agreement with their predicted value of E_I=1.1eV.

Another materials system which has been studied to investigate the optical properties of staggered lineup heterojunctions is $p-In_{1-x}Ga_xP/n-GaAs$ grown by liquid phase epitaxy (LPE). S. Julie Hsieh and co-workers reported seeing a below bandgap peak in the photovoltaic response at room temperature [3]. The half-power point of the peak was at 1.31eV and corresponded closely to their predictions for the interfacial energy gap. The predicted band lineup for this heterojunction was actually a straddling lineup rather than a staggered one.

Experimentally these lineups were measured to be staggered. This may be the result of the particular orientation of the GaAs substrate used, {111}, which may have interfacial dipoles that shift the lineup from a straddling to a staggered one. For reasons explained in a later section, we also explored these $p-In_{1-x}Ga_xP/n-GaAs$ heterojunctions as potentially superior below gap emitters.

The third materials system that has been examined to study the staggered lineup heterojunction is $p-ZnSnP_2/n-GaAs$. At room temperature we observed below bandgap peaks in both the emission and absorption spectra which we believe may be due to the below gap mechanisms discussed in the next section. Experimental values of E_I obtained from these data agreed well with the theoretical prediction of E_I obtained from the calculated band lineup. The $ZnSnP_2/GaAs$ heterojunction was the one investigated in the greatest depth and so these results will constitute the major portion of this work.

To understand some of the possible mechanisms for below bandgap absorption and emission in the staggered lineup heterojunction, let us consider the appropriate band diagrams for $p-ZnSnP_2/n-GaAs$. The flat band lineup for this heterojunction was calculated using results from

capacitance-voltage (C-V), Hall, photoconductivity, and photovoltaic measurements, which will be discussed in detail in Section 2.1. Figure 2 reveals that the flat band lineup for $ZnSnP_2$/GaAs is staggered with the conduction band minimum of the p-type $ZnSnP_2$ below that of the n-GaAs. This configuration has been referred to as the p (down)/n (up) band lineup [2]. Since $ZnSnP_2$ is grown unintentionally p-type, this configuration is the only one we have been able to achieve with this material. To investigate the opposite configuration, the n (down)/p (up) lineup, we examined the $p-In_{1-x}Ga_xP$/n-GaAs heterojunction. These results are discussed in Section 2.2.

Now examine the equilibrium band lineup of $p-ZnSnP_2$/n-GaAs in Figure 3. Charge has transferred to equilibrate the electrochemical potential throughout the heterojunction. This charge transfer creates depletion regions just as in the p-n homojunction case, except now the band offsets create barriers and form potential wells on adjacent sides of the interface. This diagram is drawn in exaggerated proportions to aid in the analysis of this section.

Consider the effect of illumination on this hetero-junction with zero applied voltage. A potential mechanism for below gap absorption might involve the excitation of an electron out of a state in the valence band well
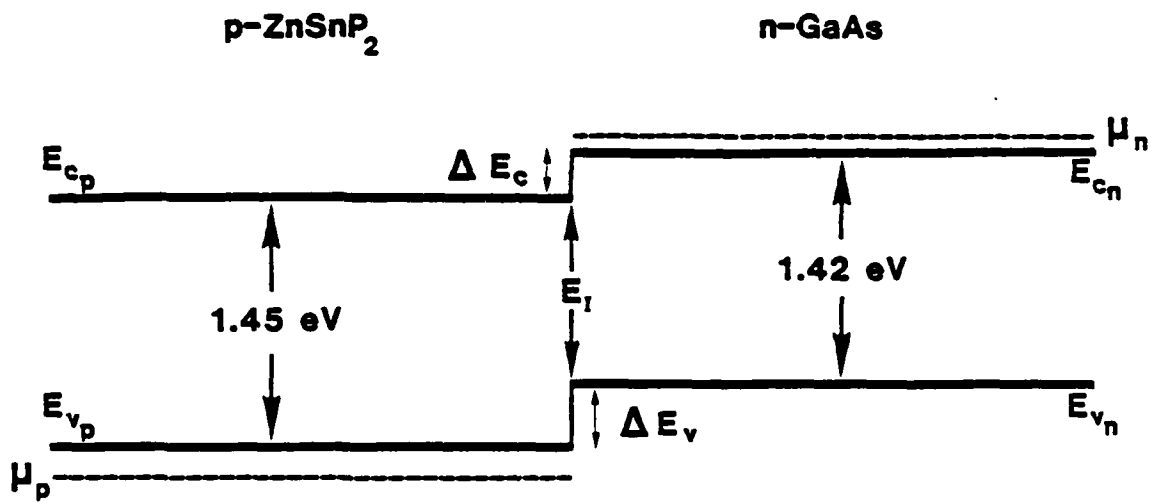
Figure 2   p-ZnSnP$_2$/n-GaAs p(down)/n(up)
            staggered lineup.
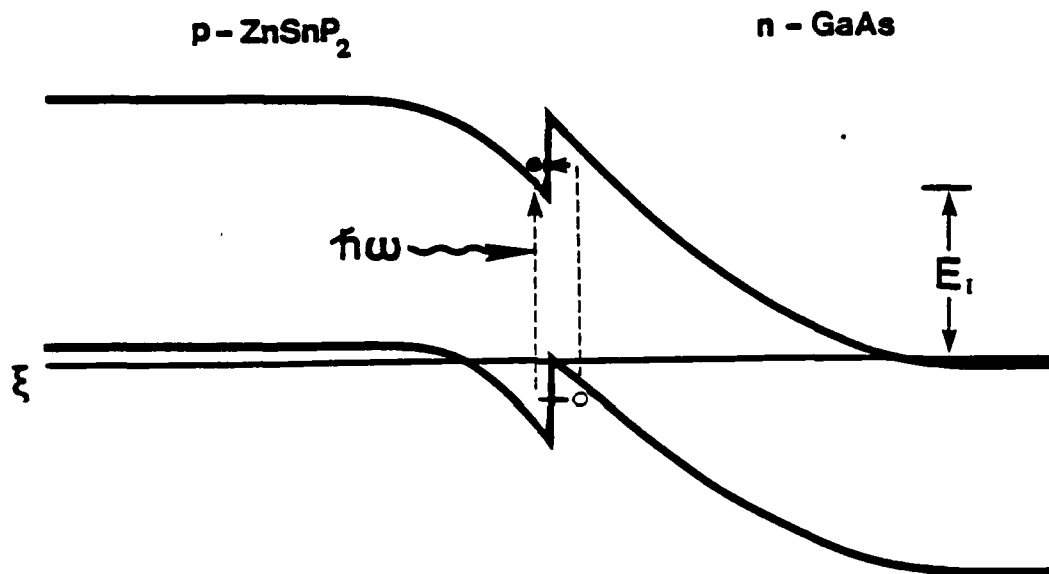
Figure 3 p-ZnSnP$_2$/n-GaAs equilibrium diagram
and below bandgap absorption mechanism.

of the n-GaAs to a virtual state in the gap. Since the electron considered quantum mechanically is a wavepacket, part of the wavepacket of an electron in a virtual state near the interface may overlap unfilled states in the conduction band well of $ZnSnP_2$. In other words, the electron may tunnel from the virtual state into unoccupied states in the $ZnSnP_2$ well. The energy of the photon absorbed therefore corresponds to the energy difference between the initial valence band state and the virtual state in the gap of GaAs. This energy, as can be seen from the diagram, is less than the energy gaps of either of the constituent semiconductors. The below gap absorption is then detected as the electrons in the conduction band well and holes created in the valence band well tunnel through their respective barriers and drift to contribute to a negative generation current.

A second mechanism would involve the tunneling of an electron out of the valence band well to a virtual state followed by excitation to the conduction band through photon absorption. This second mechanism is equivalent to hole tunneling and so is much less probable than electron tunneling due to the larger hole effective mass. This is because the tunneling probability of a carrier through a barrier decreases roughly exponentially with effective mass. For example, the tunneling probability for an

electron tunneling through a triangular barrier is,

$$P(\epsilon) = \exp\left[\frac{-4(2m^*)^{\frac{1}{2}}\Delta\epsilon^{3/2}}{3q\hbar E}\right], \tag{1.1}$$

where E is the constant electric field, ϵ is the electron energy, $\Delta\epsilon$ is the energy barrier height above ϵ, and m^* is the electron effective mass.

To examine a potential mechanism for below bandgap emission look at the heterojunction in forward bias in Figure 4. The applied voltage is indicated in terms of the potential energy difference, qV, between the quasi-Fermi levels in the field free regions of the two materials. In forward bias minority carriers diffuse over the diminished barriers and are temporarily confined in the potential wells. The electrons confined in the conduction band well of the p-ZnSnP$_2$ could then tunnel out to virtual states in the gap of GaAs and then radiatively recombine with a hole confined in the valence band well of the n-GaAs. Another mechanism would involve the electron emitting a photon and dropping from the conduction band well to a virtual state in the gap of ZnSnP$_2$. The electron could then tunnel to recombine with a hole confined in the GaAs valence band well. This second mechanism involves hole tunneling and, as is the case for absorption, would be a less likely mechanism. A previous publication [2] suggested that the opposite staggering arrangement, the
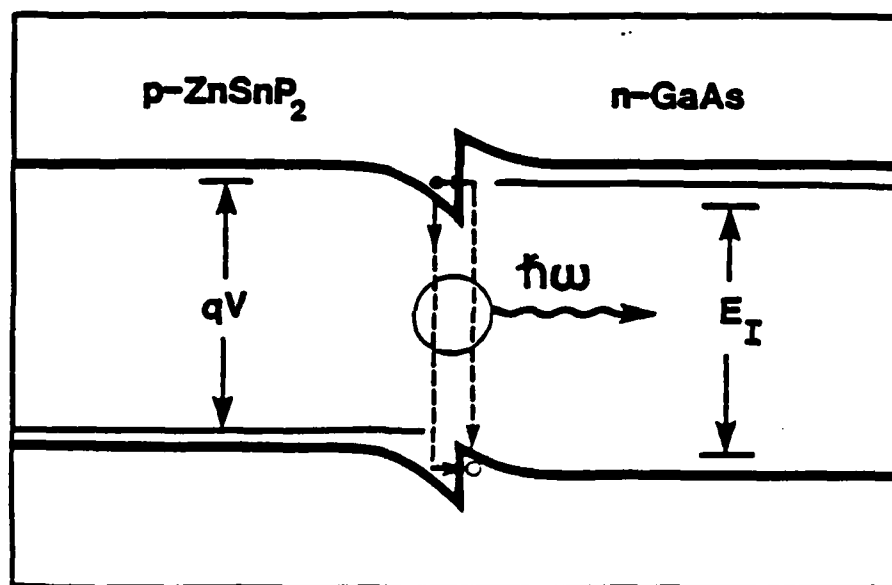
Figure 4   p-ZnSnP$_2$/n-GaAs forward bias
diagram and below bandgap
emission mechanism.

n(down)/p(up) lineup, might prove to be the most strongly
emitting lineup since in this case accumulated majority
carriers instead of injected minority carriers are involved
in the radiative recombination. Since we have not been
able to grow n-type $ZnSnP_2$, we obtained this lineup using
$p-In_{1-x}Ga_xP/n-GaAs$ heterojunctions. The results of
emission experiments on these devices will be examined
in Section 2.2.3.

2.1 ZnSnP$_2$/GaAs

2.1.1 Material Properties and Device Construction

Before considering the construction of the devices used in these investigations, it will be useful to discuss some important material properties of the somewhat unfamiliar semiconductor ZnSnP$_2$. ZnSnP$_2$ is a II-IV-V$_2$ ternary compound which can have either the disordered sphalerite or the ordered chalcopyrite crystal structure. The sphalerite structure for ZnSnP$_2$ is essentially the cubic zinc-blende structure having a face centered cubic (fcc) sublattice of P atoms and a random fcc sublattice of the Zn and Sn cations. The chalcopyrite structure is tetragonal because the cation sites are nonequivalent and ordered. The chalcopyrite structure is shown in Figure 5, where the tetragonal axis is desig- nated as the c axis. In ZnSnP$_2$, the chalcopyrite structure shows no tetragonal distortion, unlike some chalcopyrites, so that c = 2a. Using double-crystal x-ray diffraction measurements the lattice constant of ZnSnP$_2$ was determined as 5.6507 Å, which results in a lattice mismatch with GaAs of less than 0.44%. The energy bandgap of ZnSnP$_2$ was determined to be 1.45eV through differential analysis of photoconductivity data on ZnSnP$_2$ layers grown on semi-insulating (SI) GaAs substrates.
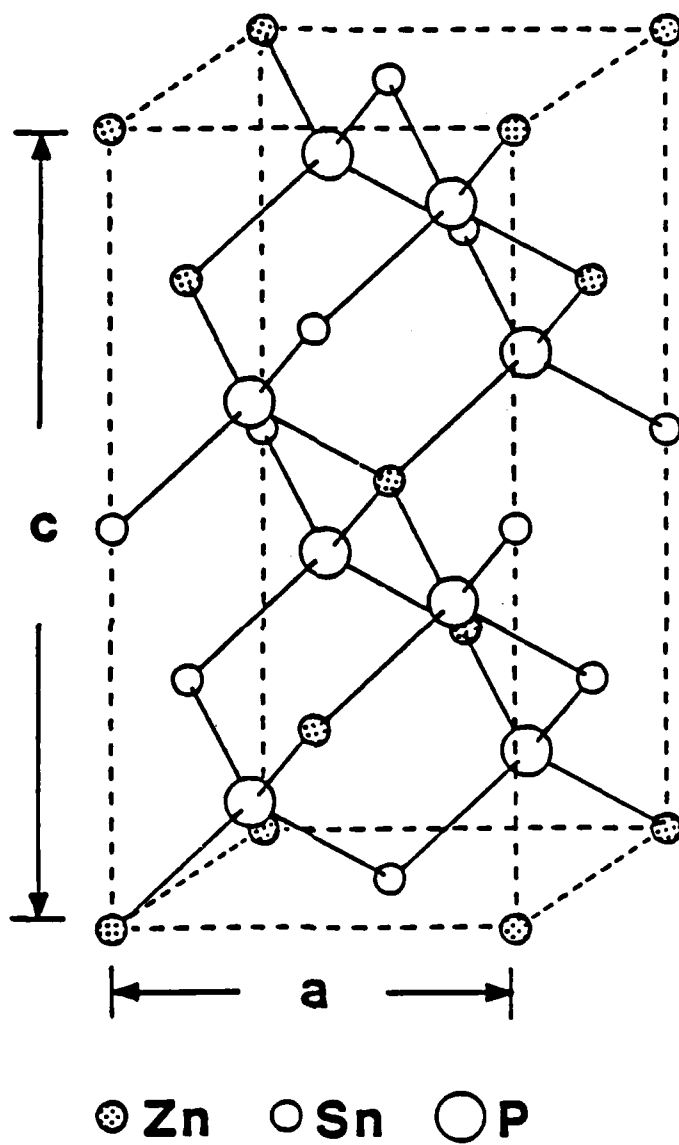
Figure 5   ZnSnP$_2$ chalcopyrite crystal
structure.

The device structure used in this work, shown in Figure 6, consisted of p^+-ZnSnP$_2$ layers grown on {211}n$^+$-GaAs substrates. The ZnSnP$_2$ layers were grown by LPE using an open tube system. These layers were grown by Gary A. Davis and the details of the growth were reported earlier [5]. The ZnSnP$_2$ was grown unintentionally p-type. The hole concentration was determined to be $p = 5 \times 10^{19}$cm^{-3} from Hall measurements performed on layers grown on SI GaAs substrates. The electron concentration of the GaAs substrate was determined using Hall measurements to be $n = 10^{18}$cm^{-3}. The bandgap of the GaAs substrates was observed by photovoltaic measurements to be 1.42eV. We also observed evidence of Zn diffusion from the epitaxial ZnSnP$_2$ into the GaAs substrates. Delineation etches of ZnSnP$_2$ layers grown on SI GaAs revealed both a growth interface and a diffusion front at about 1 μm into the substrate. This indicated that the Zn diffusion was converting a thin region of the SI GaAs substrates near the interface to p-type. When the ZnSnP$_2$ was grown on n$^+$-GaAs, the Zn diffusion was not sufficient to convert the GaAs to p-type. In this case only a single growth line was visible at the interface after the delineation etch. Microprobe analysis indicated outdiffusion of Ga into less than 1 μm of the ZnSnP$_2$ but with no type conversion. The ZnSnP$_2$ layers used in these devices were fairly thin, about 3 μm. The diodes were defined using
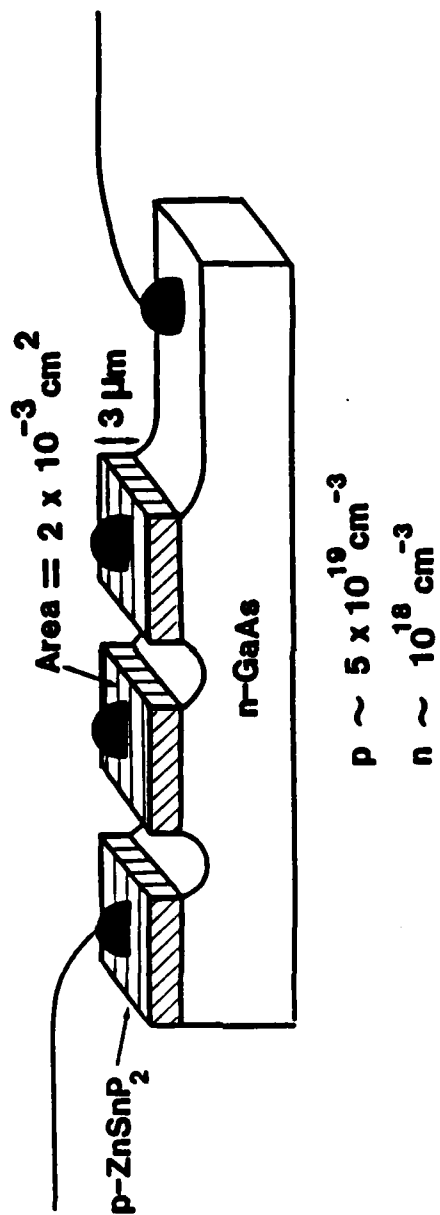
Figure 6   ZnSnP₂/GaAs device construction.

standard photolithographic techniques and were etched
down to an area of $2 \times 10^{-3} cm^2$ using Br-methanol. Finally,
10 mil Sn spheres were alloyed to both materials since
Sn forms ohmic contacts with both p-$ZnSnP_2$ and n-GaAs.

The GaAs substrates used in this work had the {211}
orientation. This choice of substrate orientation was
particularly important for two reasons. Firstly, previous
work [6] revealed that the {211} orientation of the GaAs
suppresses all but one orientation of the c-axis of the
chalcopyrite $ZnSnP_2$ layer. The c-axis of the $ZnSnP_2$ can
have three different orientations with respect to the
cubic axes of the sphalerite GaAs substrate. Where regions
having different c-axis orientations meet, an antiphase
domain boundary is produced. Antiphase domain boundaries
contribute to strain and scattering and so degrade the
mechanical and electrical properties of the material.
Back reflection Laue photographs of $ZnSnP_2$ layers grown
on several different substrate orientations were taken
to determine the substrate orientation dependence of the
c-axis orientation. The {211} orientation was determined
to suppress all but one c-axis orientation by the presence
of four asymmetric additional spots in the Laue photograph.
Therefore the {211} orientation of the GaAs substrate
best suppresses antiphase domain boundaries associated
with material regions having different c-axes.

The second reason the {211} substrate orientation
is important for this work is related to the suppression
of net interfacial charge. Arguments presented by W.A.
Harrison and co-workers [7] show that certain orientations
of polar/nonpolar or binary on elemental semiconductor
interfaces will tend to minimize interfacial charge.
These arguments can be extended to ternary on binary
interfaces. The development of these concepts is somewhat
involved, so here we present a simplified argument utilizing
Harrison's transmutation alchemy. Figure 7 shows the inter-
face between a hypothetical ternary compound $InGaP_2$ and the
binary compound GaAs. The orientation of the interface
is shown parallel to one of the <111> bond directions. Since
each plane of atoms parallel to the interface in this
case contains equal numbers of anions and cations, these
planes are on average charge neutral. Slight misorienta-
tions of this interface with respect to the <111> bond
directions will not on average introduce significant
interfacial charge since we are considering III-III-V_2 on
III-V system. Harrison points out that the tetrahedral
bond configuration assures that each of the bonds connecting
each atom to its four nearest neighbors contains exactly
two electrons. The electron distribution along each bond
depends on which species are being bonded, but the overall
bond charge remains the same. Using this argument one
can determine the overall interface charge by counting
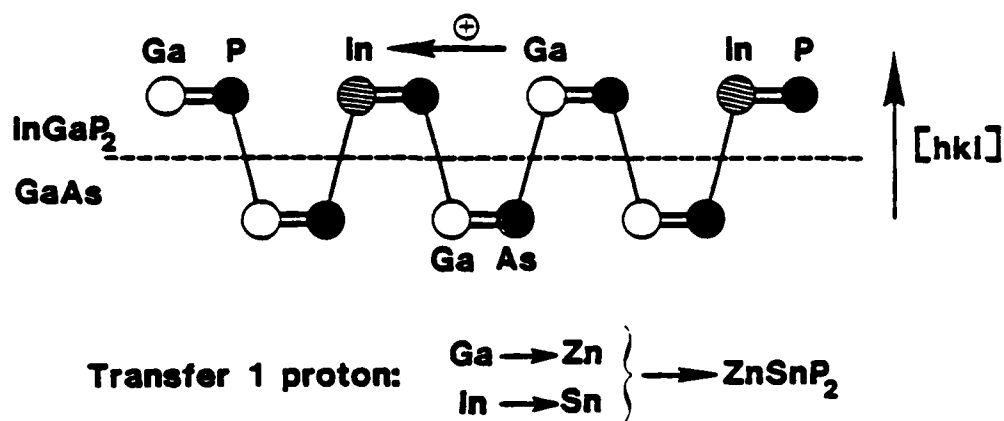
Figure 7   Charge neutral interface
            construction.

each column V atom as having +1 charge from the extra proton
relative to column IV, and each column III atom as having
-1 charge. One can see that according to this approach, in
this III-III-V_2 on III-V system, small misalignments of the
interface with respect to the <111> bond directions will
not produce significant interfacial charge.

The situation is very different for mixed column
materials systems such as the II-IV-V_2 $ZnSnP_2$ on III-V GaAs
heterojunction. To examine this case, imagine the hypo-
thetical transfer of a proton from each of the Ga atoms to
each of the In atoms as in Figure 7. This process will
transmute Ga into Zn and In into Sn thereby producing
$ZnSnP_2$ on GaAs. Assuming that the electron
configuration during this proton transfer remains
unchanged, the only charge transfer of concern is
that due to the proton movement. This ignores the part
of the electron distribution that would tend to follow
the proton motion. Therefore the real positive charge
transfer for each proton moved is less than one. For
simplicity we ignore these complications. Since the
interface is in this case parallel to the <111> bond
directions, the positive charge moves parallel to the in-
terface and so the interfacial plane remains on average
charge neutral. If we misalign the interface from the
<111> bond directions, however, there will be a component
of the positive charge motion either toward or away from

the interface. This will result in the accumulation
of positive or negative charge, respectively, at the in-
terface. The charge motion in the other parallel planes
of the top layer will on average cancel in pairs.

A mathematical way of expressing the condition for
a charge neutral interface can be stated as a relation
between the Miller indices (hkl) of the interfacial plane
and the <111> bond direction. Let [hkl] indicate the
direction perpendicular to the interfacial plane. For
the interfacial plane to be parallel to the <111> bond
directions, the [hkl] direction must be perpendicular to
that direction. This gives the condition,

$$[hkl] \cdot <111> = \pm h \pm k \pm l = 0 . \qquad (2.1)$$

The lowest index orientation that can satisfy this
condition is the {110} orientation. This is a happy
coincidence for some applications since the {110} planes
are the natural cleavage planes for III-V compounds.
Unfortunately in our case, growth of $ZnSnP_2$ on {110} GaAs
is not the best for the elimination of antiphase domain
boundaries. The next lowest index that satisfies the
charge neutral condition, the {211} orientation, is also
that which best suppresses the formation of these antiphase
domain boundaries. These are the two important aspects of
the {211} substrate orientation for our devices.

Interfacial charge is a problem in heterojunctions because among other effects, it can greatly alter the experimental determination of the band lineup. Although interfacial dipoles would be necessary to actually change the band offsets, interface charge will affect the experimental values of the band offsets derived from C-V data. These complications will be discussed further in Sections 2.1.4 and 2.3.

2.1.2 Absorption Experiments

Both absorption and emission experiments were performed at room temperature on these $ZnSnP_2$/GaAs devices to test our model of the below bandgap mechanism for absorption and emission. First we shall consider the results of the absorption experiments. The apparatus used for these experiments is shown in Figure 8. The source of monochromatic radiation incident on the heterojunction was a halogen vapor lamp focused by a toroidal mirror on the entrance slit of a Spex Minimate monochromator. The entrance and exit slits of the monochromator were set at 1.25mm to maximize resolving power while still maintaining an acceptable signal level. This slit width results in a 50Å spectral bandpass. The exit radiation was chopped at 700 Hz and was then incident on the cleaved face of the sample. This cleaved plane is perpendicular to the hetero-interface. For the photovoltaic
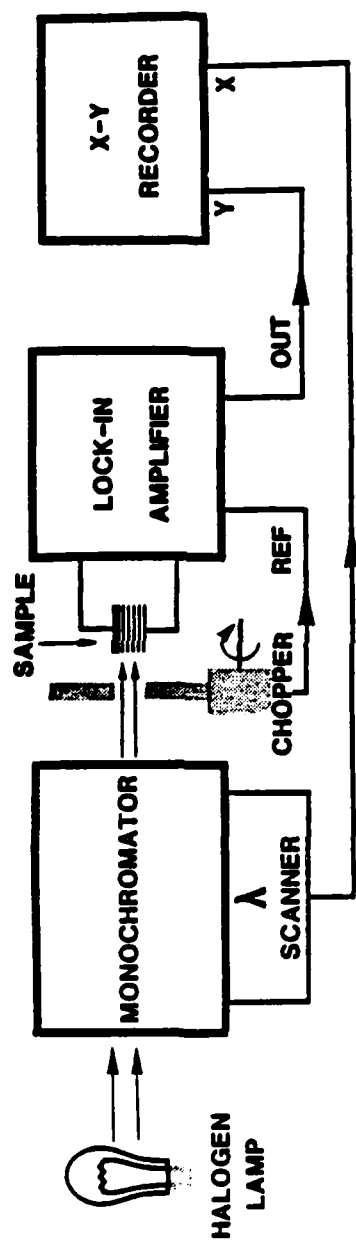
Figure 8 Absorption experiment apparatus.

experiments, no voltage bias was applied to the sample.
The ac response voltage across the sample was measured
directly by an EG&G 124A lock-in amplifier. The phase
was adjusted to maximize the signal and the time constant
was set to as low a value as possible while avoiding
excess noise. The wavelength was scanned automatically
from $0.7\,\mu m$ to $1.1\mu m$ by the wavelength drive motor. The
controlling voltage to the wavelength drive served as
the x-axis of an HP7035B x-y recorder. The chopper motor
served as the external frequency reference of the lock-in
amplifier. The lock-in output was used as the y-axis
of the x-y recorder. The wavelength was scanned in the
slow scan mode which took eight minutes to scan $\Delta\lambda = 0.4\mu m$.

The photovoltaic response as a function of photon
energy is shown in Figure 9. The scale of the x-axis
is actually linear in wavelength and not energy, but is
shown in energy units for ease of interpretation. Two
broad peaks are observed in the room temperature photo-
voltaic response. The larger peak, having a half-power
point at 1.42eV, appears to be the band-to-band absorption
peak for GaAs. Since the $ZnSnP_2$ is much more heavily doped
than the GaAs, most of the depletion region occurs in
the GaAs. In the absorption mode, the signal comes only
from those carriers created where there is a field to
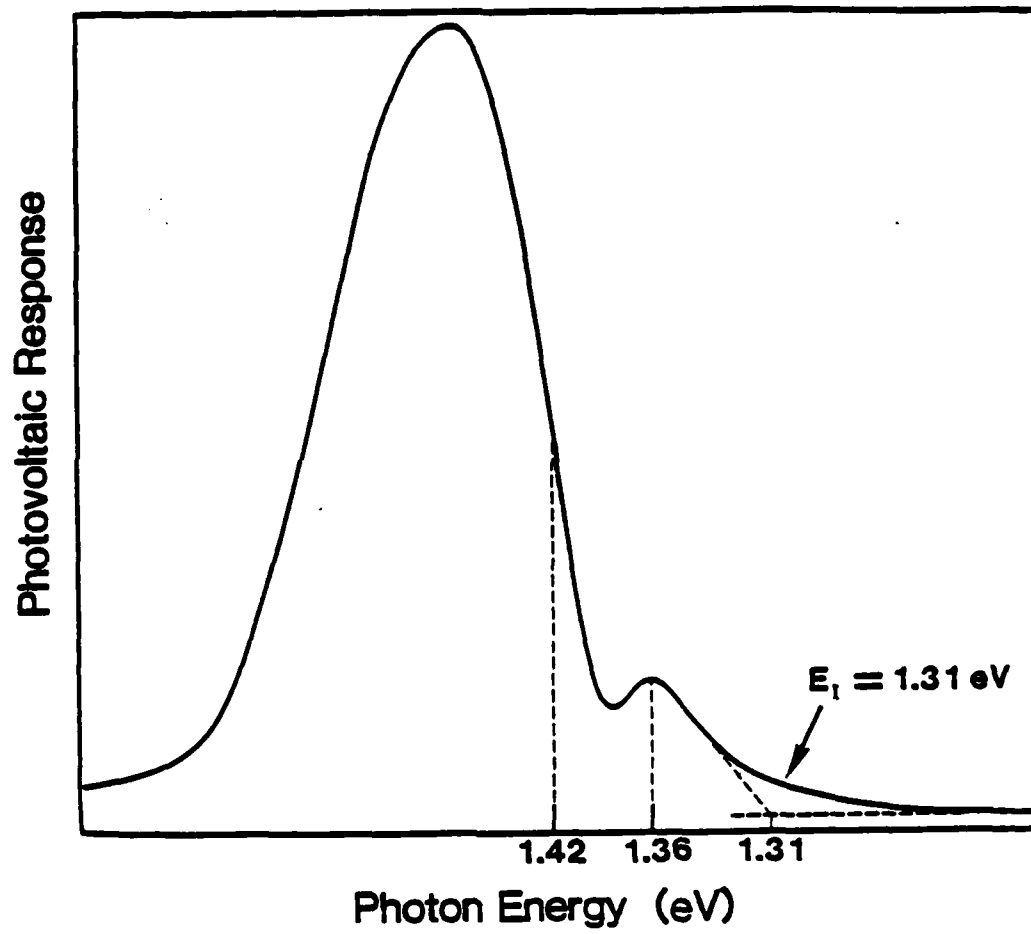
Figure 9   ZnSnP$_2$/GaAs photovoltaic response.

separate them. Therefore, the detectable absorption occurs only in the depletion region and so it is reasonable that no $ZnSnP_2$ absorption peak is observed. The smaller peak has its maximum at 1.36eV. The amplitude of this peak depends on the orientation of the hetero-interface to the incident radiation as can be seen in Figure 10. The below bandgap peak almost disappears when the radiation is incident normal to the epitaxial layer rather than to the cleaved face. The orientation of the normal to the cleaved face with respect to the incoming light varied from $0°$ to $45°$ for maximum signal. These results may indicate that the below gap absorption depends on the polarization of the incident light with respect to the interface. The largest below gap response occurs when the polarization is in a plane perpendicular to the interface, or when the light is incident parallel to the interface.

If we assume that this below bandgap absorption peak is due to the mechanism that has been described, one can extract an estimate of the interfacial energy gap E_I from the absorption data. Looking back at Figure 3, it is evident that no significant absorption will take place at energies below the interfacial energy gap E_I since this would involve highly improbable tunneling. Therefore to extract E_I from the below gap peak it is not appropriate to use either the maximum or half-power point energies.
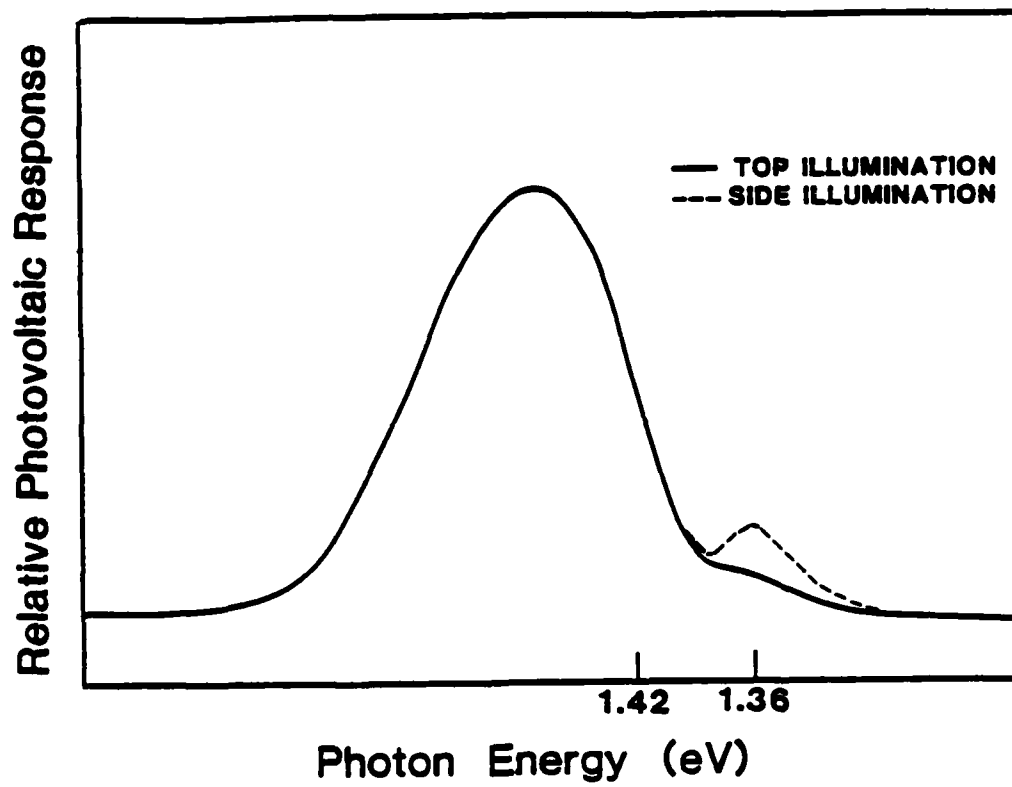
Figure 10   Orientation dependence of illumina-
tion on below bandgap photoresponse.

To estimate E_I roughly we can extrapolate the steepest part of the below gap peak to the zero absorption line. This results in an approximation of $E_I = 1.31eV$. It appears that E_I may be even smaller than this since absorption is observed below this energy.

We also performed absorption measurements with the sample in reverse bias. A dc voltage was applied to the sample in series with a load resistor. The signal was taken directly off the series resistor and fed into the lock-in amplifier. These results are shown in Figure 11 as a family of curves for biases from 0 to -1.6 V separated by equal voltage increments (0.4V). Both the high energy absorption and the below gap peak increase with increasing reverse bias. The increase in the high energy response may be due to an increase in the tunneling of electrons through the conduction band notch into the GaAs where the electrons were excited from the valence band of $ZnSnP_2$. This explanation is reasonable since tunneling increases with field and so reverse bias. The below bandgap absorption should also increase with increased field in the interfacial region. There is also a shifting of the peak of the below gap response with reverse bias. This may be due to the change in the quasi-Fermi levels with reverse bias. As reverse bias is increased, minority carriers are extracted from the interfacial region. This results in fewer electrons or filled states in the
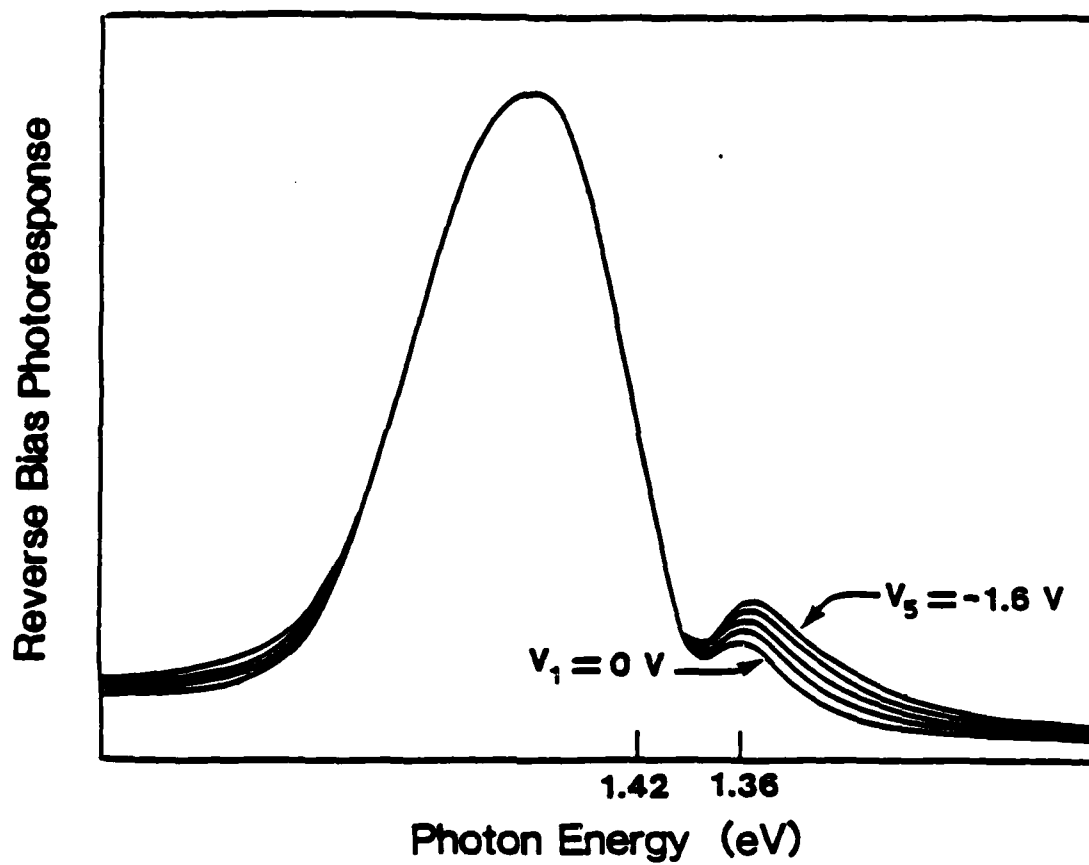
Figure 11   ZnSnP$_2$/GaAs reverse bias photoresponse.

conduction band well of $ZnSnP_2$ and fewer holes in the valence band well of GaAs. This allows absorption at lower energies and so shifts the below bandgap peak to longer wavelengths.

2.1.3 Emission Experiments

Next we conducted room temperature emission experiments on these $ZnSnP_2$/GaAs heterojunctions. A block diagram of the apparatus used in these experiments is shown in Figure 12. This apparatus was the product of an evolution of attempts to measure the emission spectra of these devices. Short range emission measurements without the monochromator were made with a PbS photoconductive cell held at liquid N_2 temperature. The PbS cell was selected since it has detection capability at wavelengths greater than 4μm. A GaAs filter placed in front of the PbS cell indicated that there was significant emission below the absorption edge of GaAs. The PbS cell appeared to be too insensitive to pick up the emission when filtered through the monochromator. A Si p-i-n photodiode also proved to be too insensitive. The emission from the heterojunction with constant forward current bias of 20 to 100mA or current density of 10 to $50A/cm^2$ could be seen with an infrared (IR) viewer. The IR viewer was used to line up the heterojunction emission onto the entrance slit of the monochromator.
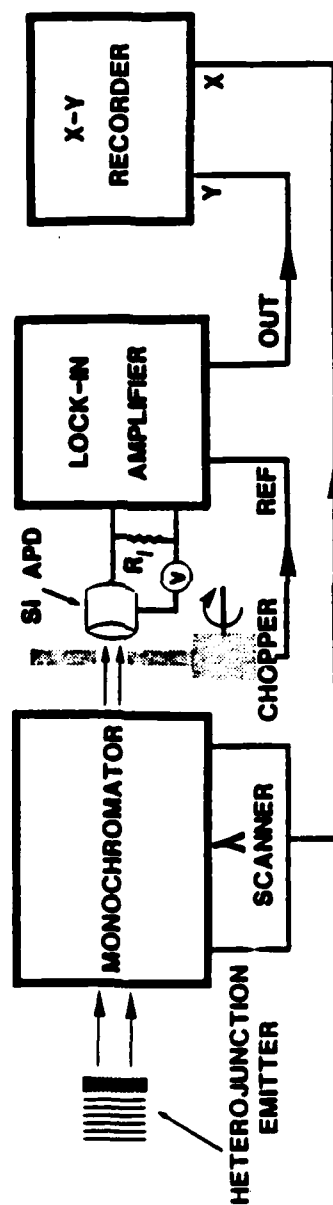
Figure 12 Emission experiment apparatus.

The last detector used was a Si avalanche photo diode (APD). Despite the fact that the Si absorption cuts off at a fairly short wavelength, around 1 μm, the increased sensitivity of this detector made it the best available for our experiments. The apparatus for the emission experiments was then set up using the Si APD as shown in Figure 12. The heterojunction was positioned in place of the halogen vapor lamp using a two degree of freedom micromanipulator. The heterojunction emission was focused with a toroidal mirror onto the entrance slit of the monochromator. There was some orientation dependence of the emission with the largest signal detected when the normal to the epitaxial layer pointed directly into the toroidal mirror. The exit emission from the monochromator was chopped at 700 Hz and then focused onto the Si APD. The Si APD was biased appropriately just into avalanche. The ac signal across a 47kΩ series resistor housed in a shielded box was fed into the lock-in amplifier. The lock-in amplifier was operated in the differential mode with careful grounding of the detection circuitry to ensure maximum signal to noise ratio. The calibration of the monochromator and alignment of the Si APD was checked using a He-Ne Laser.

A set of emission curves for one of the heterojunction emitters is shown in Figure 13. The sample was biased at
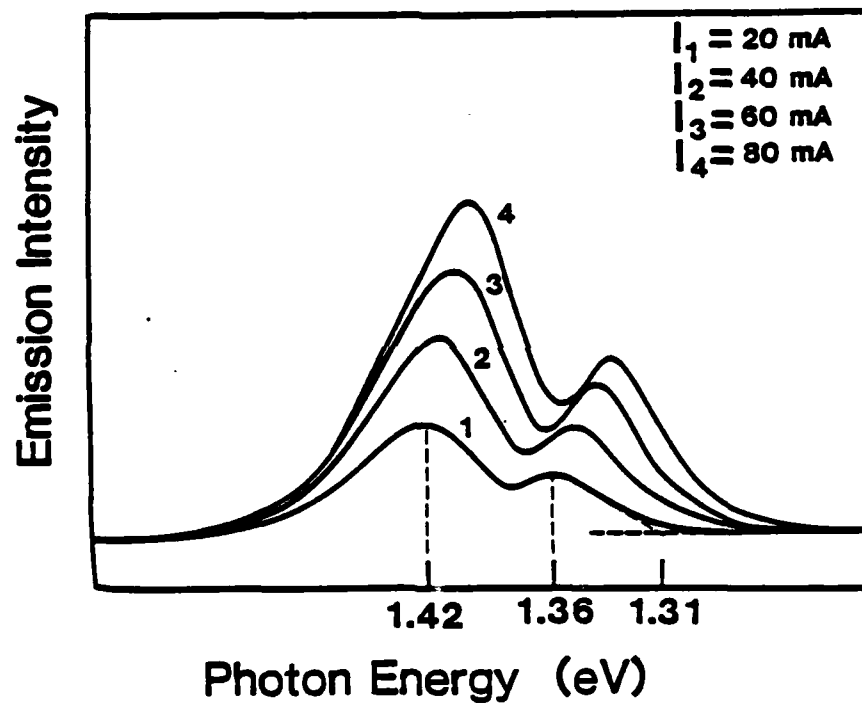
Figure 13   ZnSnP$_2$/GaAs emission spectra
at four constant current
densities.

constant current densities of 10, 20, 30, and 40A/cm^2.
Two peaks are observed in the emission. Consider the
emission peaks at the lowest current bias of 10A/cm^2.
Here the slightly larger peak has its maximum at 1.42eV.
This peak appears to be the band-to-band emission peak
for GaAs. We see no analogous emission peak for ZnSnP$_2$.
This can be explained in a similar fashion as for the
absence of a ZnSnP$_2$ peak in the absorption. Since the
ZnSnP$_2$ is much more heavily doped than the GaAs, many more
holes are injected into the GaAs well than electrons into
the ZnSnP$_2$ well. Therefore, there are many more minority
carriers available in the GaAs which are necessary for
the band-to-band radiative recombination.

The smaller emission peak has its maximum at 1.36eV.
If we again assume our below gap emission mechanism is
correct, an estimate of E_I can be extracted from this peak.
As in the case for absorption, one would not expect to
see significant emission below E_I if the forward bias
diagram is correct. We can, therefore, estimate E_I by
extrapolating the steepest part of the below gap emission
peak to the zero emission line. This results in an esti-
mate of E_I = 1.31eV which again is an upper limit. This
is the same value of E_I as that obtained from the absorp-
tion data.

Some other points of interest concerning these emission data should be mentioned. One notices immediately that the two emission peaks are much closer in height than those of the absorption data. In the case of absorption, the active region for the band-to-band GaAs absorption is the depletion region. Using the depletion approximation the depletion width was estimated at 500 Å. The active region for the below gap absorption is much smaller than this because it is the width of the region across which significant tunneling can occur. This is likely to be a few lattice constants in width or a few tens of Å. One would therefore expect the below gap absorption peak to be approximately an order of magnitude smaller than the band-to-band absorption peak. In the case of emission, the below gap and band-to-band mechanisms are both controlled by the supply of holes injected into the GaAs well. These holes are involved in the radiative recombination of both mechanisms. Therefore, it is reasonable that the emission peaks are closer in height than those of the absorption spectra.

Another point of interest is the shift of the two emission peaks to longer wavelengths at increased current bias. The most likely cause of this shift is heating of the sample since the bandgaps of both semiconductors decrease with increasing temperature. The shrinking of the

bandgap corresponds to an increase of the lattice constant.
Double-crystal x-ray diffraction measurements indicate no
difference in the thermal expansion between $ZnSnP_2$ and
GaAs from room temperature to about 150°C. Since the
lattice constants on both sides of the interface expand
together at the same rate, we expect to see the two
emission peaks move at about the same rate with respect
to current, as seen in Figure 13. One can estimate the
temperature changes necessary for the apparent energy
gap variations using the approximate relation,

$$E_g(T) = E_g(0) - \frac{\alpha T^2}{T+\beta} \cdot \qquad (2.2)$$

For GaAs, the empirically determined constants are
$\alpha = 5.405 \times 10^{-4}$, $\beta = 204$, and $E_g(0) = 1.519eV$ [8]. For
a constant current density 20 A/cm^2, the energy gap of
GaAs shifted from the 300K value of 1.42eV to 1.41eV.
Inserting $\Delta E_g = 0.01eV$ into equation (2.2) and solving the
quadratic yields $\Delta T = 27.4K$. So for all values of current
density used in these experiments, the temperature of
the device should remain under 150°C. Therefore, the
behavior of the emission peaks is consistent with that
expected from device heating.

Now compare the absorption and emission results
directly by examining Figure 14. Here the higher solid
curve is the photovoltaic response whereas the lower
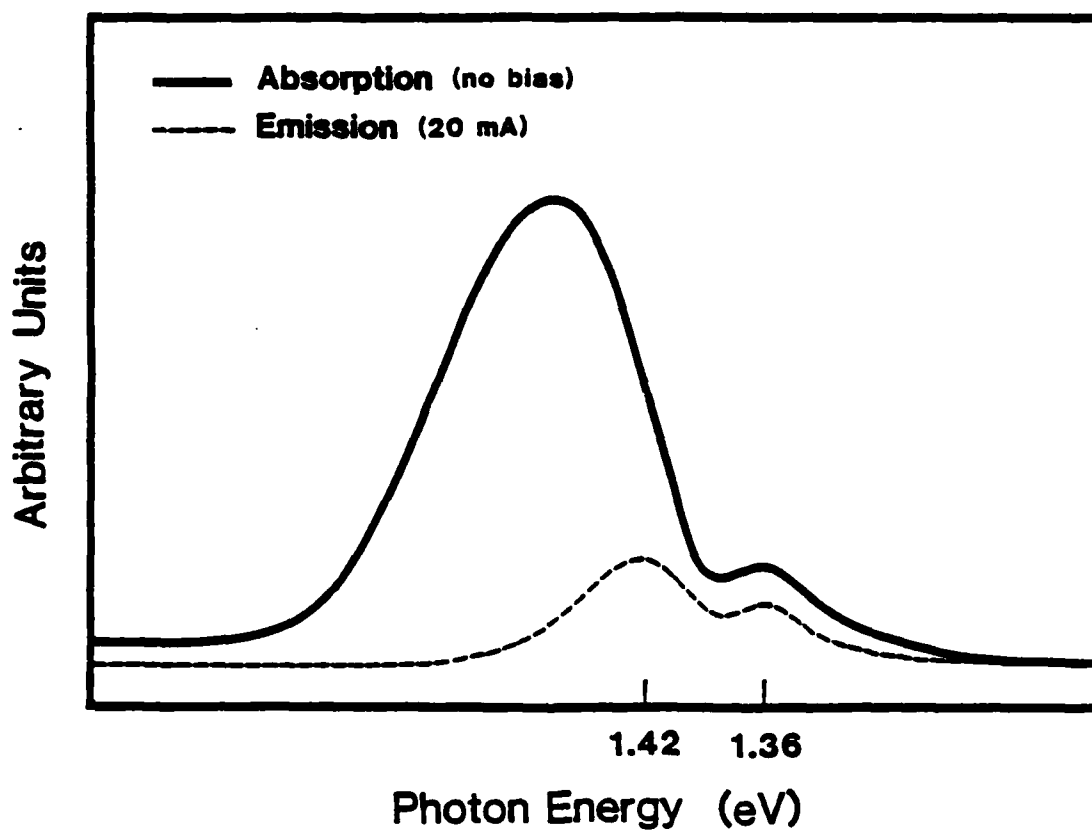
Figure 14 Overlay of photovoltaic response and low bias emission for ZnSnP$_2$/GaAs.

dashed curve is the emission spectrum at the lowest current

bias of $10 \, A/cm^2$. The higher energy emission peak has its

maximum at the half-power point energy of the larger absorp-

tion peak. One expects this type of relation between

absorption and emission for a band-to-band transition.

The energies of these peaks are appropriate for GaAs.

The below bandgap peaks in the emission and absorption

spectra are coincident in energy. This observation may

help to address an obvious concern in analyzing these

data. There is the possibility that the below gap peaks

are not due to the mechanisms described but rather to

transitions involving tunneling to and from impurity levels

in the gap. The energy coincidence of the two below gap

peaks might be taken as evidence against an impurity inter-

pretation. When optical transitions of electrons involve

impurity levels, in principle one expects a shift between

the absorption and emission peaks, where the emission peaks

at longer wavelengths. This shift is due to the Franck-

Condon principle [9,10] which states that electron

transitions are so fast that the lattice can be viewed

as static during the transition. These issues will be

addressed in Section 2.4.

2.1.4 Band Lineup

The analysis of the emission and absorption data

in Sections 2.1.2 and 2.1.3 has been based on the assumption

that the band lineup of p-ZnSnP$_2$/n-GaAs is staggered. To
show that the lineup is indeed staggered and so extract
a theoretical value of E$_I$, we need to measure several
parameters of the materials themselves as well as of the
heterojunction as a whole.

To construct the band lineup, we first determined
the built-in potential V$_o$. The built-in potential is
the difference between the chemical potentials of
the two materials or the potential that arises across
the heterojunction from charge that transfers to equilibrate
the electrochemical potential throughout the device. We
used the C-V intercept method to determine V$_o$.

For an abrupt heterojunction of area A and doping
N$_a$ and permittivity ϵ_p for the p-type material and
N$_d$ and ϵ_n for the n-type material, one can derive the
relation,

$$c^{-2} = \frac{2(\epsilon_p N_a + \epsilon_n N_d)(V_o - V)}{q \epsilon_n \epsilon_p A^2 N_d N_a} . \tag{2.3}$$

This equation reveals a linear relationship between c^{-2}
and the applied potential V [11]. The built-in potential
V$_o$ is obtained by extrapolating the c^{-2}-V plot to $c^{-2} = 0$
where the voltage intercept is V = V$_o$. This expression
neglects the effects of interface charge. Interface charge
effects will be discussed later in this section, and in
Section 2.3.

Capacitance versus voltage measurements were performed using a Boonton 72BD capacitance meter. The Boonton meter operates at 1 MHz. The capacitance of the leads and sample holder were nulled out using a nulling circuit in the Boonton meter. The sample was reverse biased out to -2 volts, beyond which the sample went into breakdown. A plot of C^{-2} versus V for these samples is shown in Figure 15. The slope and the intercept were determined using linear regression analysis. The built-in potential was determined as $V_o = 1.75$ V.

Before proceeding to construct the band lineup, let us compare this measured value of V_o with a calculated value. As mentioned earlier, the built-in potential is the difference between the chemical potentials μ_n and μ_p in the two materials,

$$qV_o = \mu_n - \mu_p . \tag{2.4}$$

Adding and subtracting the band edge energies yields,

$$qV_o = (\mu_n - E_{c_n}) + E_{c_n} - E_{v_p} - (\mu_p - E_{v_p}). \tag{2.5}$$

Since both semiconductors are degenerately doped, to determine the terms in parentheses we must use the following expressions for nondilute solutions,

$$n_n = N_{c_n} F_{\frac{1}{2}} \left(\frac{\mu_n - E_{c_n}}{kT} \right) \tag{2.6}$$
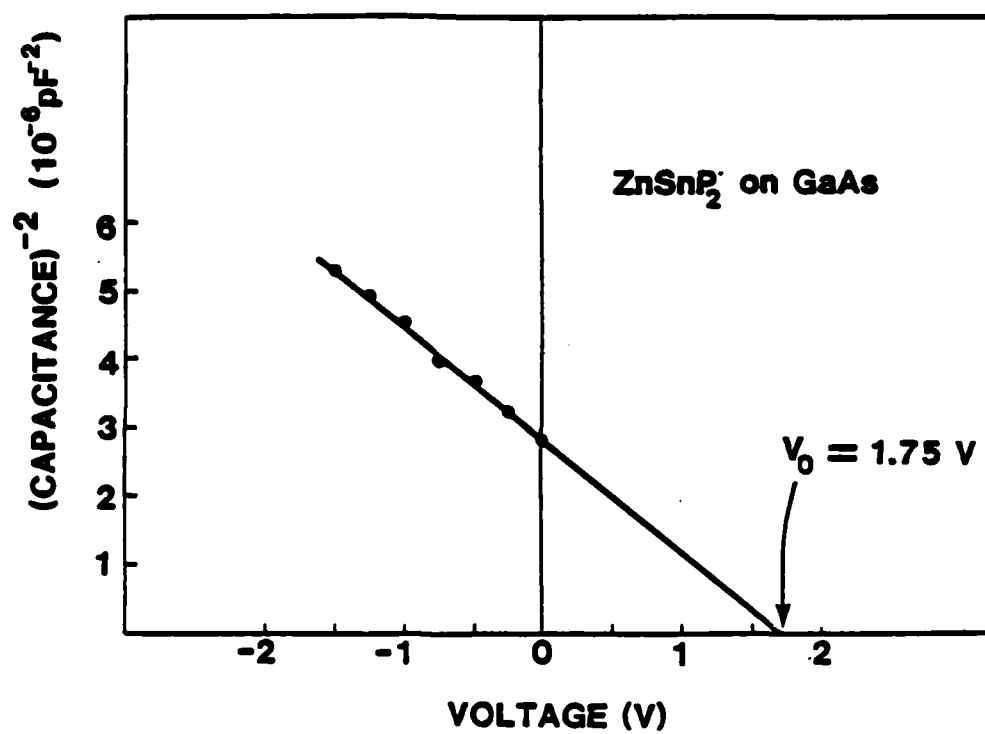
Figure 15   ZnSnP$_2$/GaAs C^{-2}-V plot shows
         V$_0$ = 1.75 V at 1 MHz.

and

$$p_p = N_{v_p} F_{\frac{1}{2}} \left(\frac{E_{v_p} - \mu_p}{kT} \right), \tag{2.7}$$

where

$$F_{\frac{1}{2}}(\eta_f) = \int_0^\infty \frac{\eta^{\frac{1}{2}} d\eta}{1 + \exp(\eta - \eta_f)} \tag{2.8}$$

and

$$N_{c_n} = 2 \left(\frac{2\pi m_e^* kT}{h^2} \right)^{3/2}. \tag{2.9}$$

Inverting equations (2.6) and (2.7), equation (2.5) becomes,

$$qV_o = E_{c_n} - E_{v_p} + kT \left[F_{\frac{1}{2}}^{-1}(\frac{n_n}{n_{c_n}}) + F_{\frac{1}{2}}^{-1}(\frac{p_p}{N_{v_p}}) \right]. \tag{2.10}$$

Now if one assumes for this calculation that the lineup is staggered, then a glance at the flat band diagram of Figure 2 shows that,

$$E_{c_n} - E_{v_p} = \Delta E_v + E_{g_n}, \tag{2.11}$$

and

$$\Delta E_v = \Delta E_c + \Delta E_g.$$

Before making a determination of ΔE_v, we should mention some of the controversies associated with determinations of band offsets. One of the oldest methods for determining the conduction band offset is through the use of the electron affinity rule [12]. This states that ΔE_c is equal to the

difference in the electron affinities of the two semiconductors,

$$\Delta E_c = x_1 - x_2 = \Delta X. \tag{2.12}$$

This method is plagued with fundamental and practical problems. On the practical side, one is attempting to determine a relatively small number, ΔE_c, on the order of a few tenths of an eV from two much larger numbers, x_1 and x_2, which are typically a few eV in size. If there is any significant error in the values of x_1 and x_2, ΔE_c will have an error on the order of its own magnitude. Also, there is evidence that the electron affinity values (x) may depend on the crystallographic plane for which they were measured. The x for a particular semiconductor for the proper orientation may not be available.

Problems exist with this "rule" on a more fundamental level. The electron affinity is essentially a property encompassing aspects of both the bulk of the semiconductor and its surface. When an electron passes from one semiconductor to the other in a heterojunction, however, the surface effects are eliminated and replaced by interface effects. So we chose to approach the band offset determination by considering the bulk rather than the surface properties of the two semiconductors. We approximated the valence band offset as the difference in the ionization energies of the semiconductors,

$$\Delta E_v = \Delta I. \tag{2.13}$$

This assumes that no interfacial dipole is formed when the two materials are joined. The ionization energy is defined as the energy difference between the top of the valence band and the vacuum state. The measured ionization energy is related to surface properties and is usually only available for natural cleavage planes for each semiconductor. To approach the ionization energy as a bulk property, we derived the ionization energies of $ZnSnP_2$ and GaAs using a dielectric two-band model [13,14,15]. The results of that calculation are

$$I_{ZnSnP_2} = 5.91eV$$

and

$$I_{GaAs} = 5.68eV.$$

This gives $\Delta E_v = 0.23eV$. To complete the calculation of V_o, we need to insert values for the carrier concentrations and the appropriate effective densities of states. Inserting the electron effective mass for GaAs, $m_e^* = 0.0665m_o$ [16], into equation (2.9) for the effective density of states one obtains for GaAs, $N_{c_n} = 4.3 \times 10^{17} cm^{-3}$.

An approximation for the hole effective mass for $ZnSnP_2$ is necessary since no experimentally determined values are currently available. Using a theoretical value determined by Goryunova and co-workers [17] of $m_h^* = 0.39m_o$, the effective density of states of the valence band of $ZnSnP_2$ is calculated as, $N_{v_p} = 6.1 \times 10^{18} cm^{-3}$.

Using the carrier concentrations determined by Hall measurements of $n_n = 10^{18} cm^{-3}$ and $p_p = 5 \times 10^{19} cm^{-3}$, and the Fermi Dirac integrals from tables, the built-in potential is calculated as, $V_o = 1.81$ V. This is in good agreement with the value obtained from the C-V data (1.75V), considering the approximations made in this calculation.

There is a fundamental problem with the C-V intercept method of determining V_o. Equation (2.3) between C^{-2} and V neglects the effects of interfacial charge. An expression for C^{-2} which is valid in the presence of voltage independent interface charge has been derived [18]. This analysis shows that interfacial charge reduces the measured value of V_o regardless of the sign of the charge. All of our C-V measurements for $ZnSnP_2/GaAs$ devices yielded linear C^{-2}-V plots. Earlier researchers presumed this linearity ensured that interfacial charge was insignificant. In fact, interfacial charge will shift the intercept $V = V_o$ to smaller values but will not affect the slope of the line. Based on this information, we believe the most accurate measured value of V_o would be the largest one we obtained. The measured V_o values ranged from 1.33 to 1.75 V. All V_o values obtained from the C-V data except the smallest value of 1.33 V, confirm the staggered lineup of $p-ZnSnP_2/n-GaAs$. Despite the fact

that ideally we are dealing with a charge neutral orientation, real substrate orientations can only be prepared accurately to $\pm 0.5°$. This small misorientation can result in significant interfacial charge in our heterojunctions. Considering this we shall use the value of $V_o = 1.75$ V for our band lineup calculation.

We now calculate the band lineup of $p\text{-}ZnSnP_2/n\text{-}GaAs$ to show that it is indeed staggered and to provide a prediction for the interfacial energy gap E_I. Looking back at Figure 2 (the flat band diagram for this heterojunction) one sees that E_I can be calculated if we obtain the band offsets and the separation of the appropriate band edges from the chemical potentials in the two materials.

Inverting equations (2.6) and (2.7) for the degenerate carrier concentrations we obtain,

$$\mu_n - E_{c_n} = kT \, F_{\frac{1}{2}}^{-1}\left(\frac{n_n}{N_{c_n}}\right) = 0.0325 \text{ eV},$$

$$E_{v_p} - \mu_p = kT \, F_{\frac{1}{2}}^{-1}\left(\frac{p_p}{N_{v_p}}\right) = 0.1225 \text{ eV}.$$

From the flat band diagram it is apparent that,

$$\Delta E_v = qV_o - (\mu_n - E_{c_n}) - E_{g_n} - (E_{v_p} - \mu_p). \qquad (2.14)$$

This results in $\Delta E_v = 0.175$ eV. Also we find
$\Delta E_c = \Delta E_v - \Delta E_g = 0.145$ eV.

Now the interfacial energy gap can be calculated as,

$$E_I = qV_o - (\mu_n - E_{c_n}) - \Delta E_c - \Delta E_v - (E_{v_p} - \mu_p).$$

This results in $E_{I_{Th}} = 1.275$ eV. This is also in good

agreement with the experimental value of $E_{I_{EX}} = 1.31$ eV.

As mentioned before, the true experimental value of E_I

is probably even smaller than that indicated by the extra-

polation of the data and so the theoretical value may

be more accurate than it appears. Still, it is necessary

to address the problems in our interpretations of the

data, since other explanations cannot be ruled out. These

will be discussed in the conclusions section.

2.1.5 Other Results

Other experiments were performed on these devices

to understand various properties of the hetero-interface.

These efforts were primarily aimed at measuring device

capacitance as a function of frequency and illumination.

Here the procedures and results of these experiments are

discussed along with suggestions for improvements for

future investigations.

There are several nondestructive electrical techniques

involving the measurement of capacitance to obtain infor-

mation about impurity concentrations and trap levels in

semiconductor devices [19]. For instance, a small

ac voltage applied to a device can cause the charging and discharging of trap levels, thereby affecting the device capacitance. One popular technique, used in the analysis of an oxide-semiconductor interface involves sweeping the Fermi level past interface state energy levels by changing the applied bias. This will cause the occupancy of the trap state to change and so will contribute to the capacitance and conductance of an MOS device. Also, the charging and discharging of interface states may be rate limited because of their relaxation times. This will result in a frequency dependence of the capacitance associated with interface states. We reasoned that these ideas and techniques might also be applicable to the characterization of interface states and charging mechanisms in a heterojunction. These different mechanisms may have different frequency dependences which we hoped to decipher. Since the occupation of interface states as well as the number of free carriers can be affected by illuminating the sample, we also conducted photocapacitive experiments at different frequencies.

Before setting up for variable frequency capacitance experiments, we first performed simple experiments to see the general effect of light on device capacitance at discrete frequencies using available capacitance meters.

First using an HP4261A LCR meter, we measured the change in
device capacitance at 1 kHz as a function of the incident
wavelength from 0.7 to 1.0 μm. The results are shown in
Figure 16. These data were obtained by shining unchopped
monochromatic light on the sample and reading the capaci-
tance directly off the HP meter. Since application of dc
light bias is very similar to the application of dc voltage
bias, the HP meter had to be used in the configuration
appropriate for C-V measurements. This entailed the in-
sertion of a 1.1 μF blocking capacitor between the high
current and voltage terminals. The HP meter cannot pro-
cess a dc current as was easily verified by shorting these
terminals together. In this configuration, the dark capa-
citance was correctly determined but no change in C was
registered when the sample was illuminated.

The wavelength was varied in increments of 10 nm using
a slit width of 1.25 mm which limits the resolution to
±2.5 nm. At 1 kHz the capacitance appears to have a spec-
tral variation very similar to that of the absorption data
with peaks at 1.44 eV and 1.36 eV. To extract the capaci-
tance of the device, the HP meter modelled these samples
as an ideal capacitance in parallel with an ideal resis-
tance. The meter determined and displayed the capacitance
and dissipation factor. For a parallel RC circuit, the
dissipation factor is equal to $D = 1/(\omega R_p C_p)$. From D at
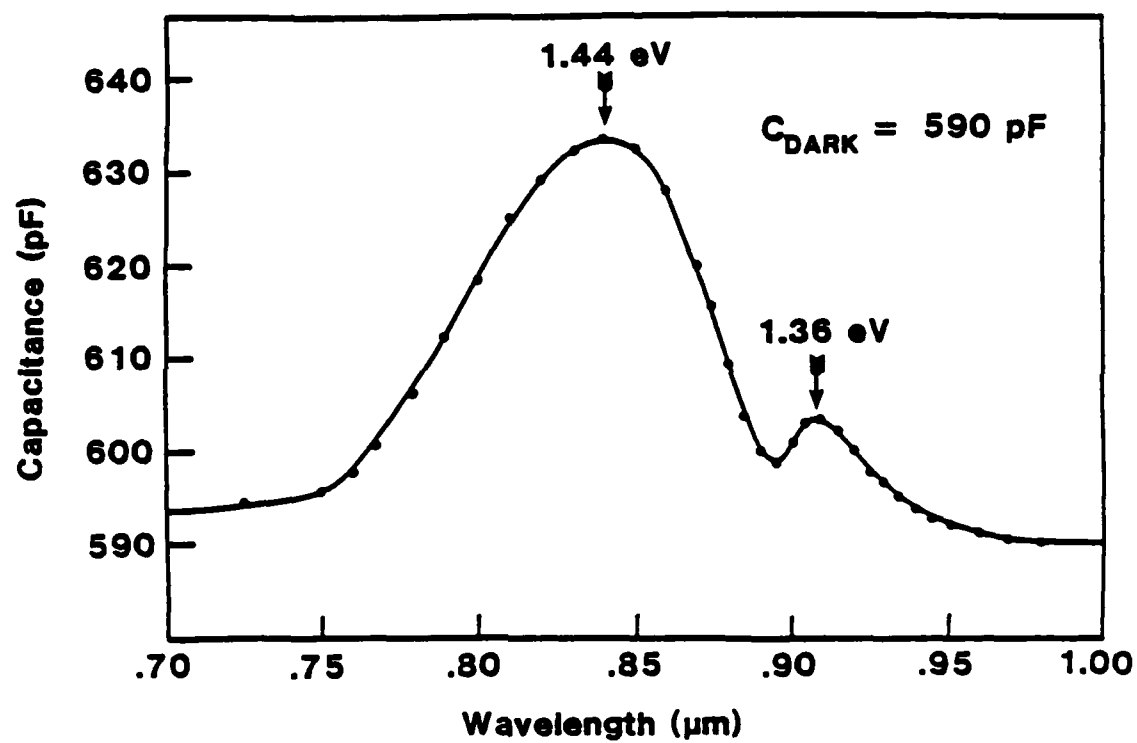
Figure 16   Capacitance as function of
photon energy of $ZnSnP_2/GaAs$
at 1 kHz.

each wavelength, the conductance $G_p = 1/R_p$ was obtained and is plotted in Figure 17. The conductance and capacitance spectra are very similar except that the conductance peaks are broader. Capacitance and conductance spectra at a single frequency such as these could not provide concrete evidence to support or refute our below bandgap model. We needed therefore to explore these spectra at many frequencies.

The HP meter also has a 120 Hz frequency setting. The capacitance of these devices at 120 Hz fluctuated wildly and the dissipation factor was off-scale. The expression for the dissipation factor reveals the problem. At low frequencies the dissipation factor becomes too large for the measurement of C to be accurate. To resolve the problem, a large parallel capacitance was added across the sample. The variation of C with λ at 120 Hz was determined in this manner to be roughly the same as that at 1 kHz.

A Boonton capacitance meter was used to perform capacitance measurements at 1 MHz. Very little change in the capacitance with illumination was observed. This result is probably due all or in part to the measurement configuration of the Boonton meter rather than the sample itself. The Boonton meter is housed in a cabinet with the necessary electronics to perform C-V measurements. The
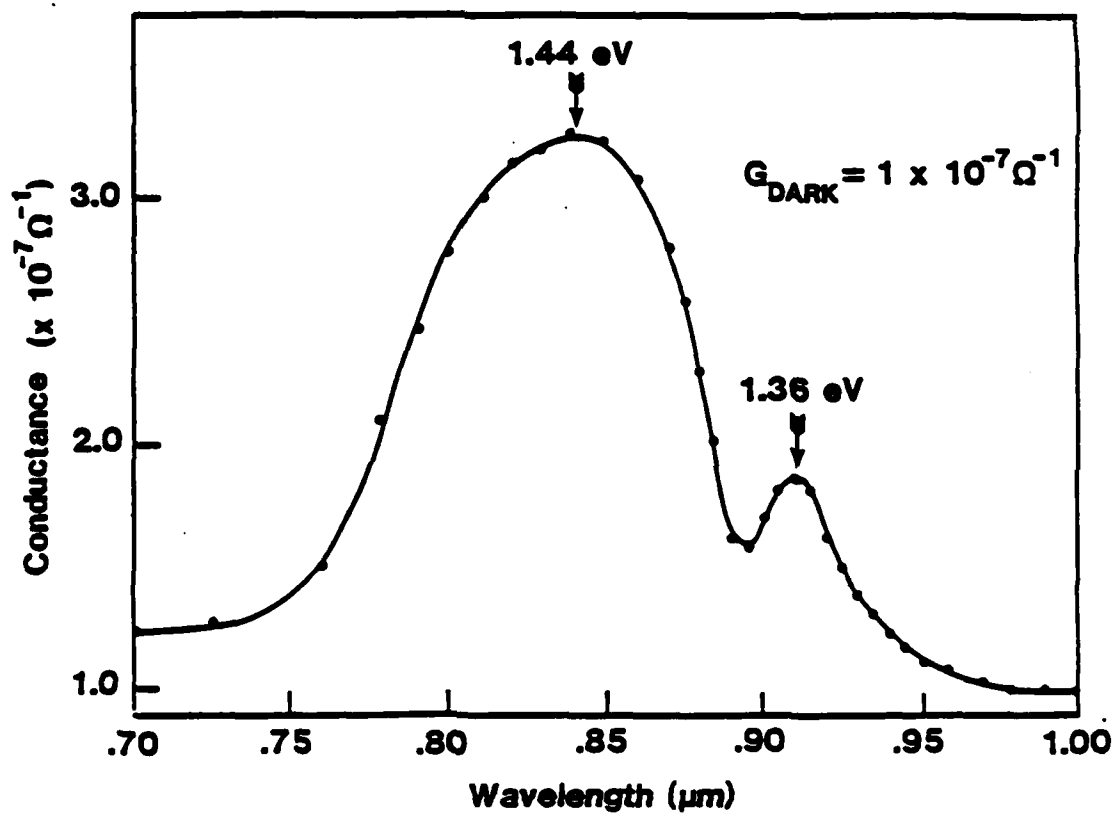
Figure 17   Photoconductance at 1 kHz for
            ZnSnP$_2$/GaAs taken from dissipa-
            tion measurements.

device capacitance is measured by the Booton with a two terminal configuration. Unless some modifications are made, this configuration probably will not detect changes in the capacitance which contribute to a dc current.

To measure the capacitance of these devices over a wide frequency range both with and without illumination, we chose to implement a technique using a lock-in amplifier. The EG&G lock-in has its own internal reference oscillator which can generate sine waves of frequencies from 0.2 Hz to 210 kHz. The capacitance measurement configuration is shown in Figure 18. The internal ac refervoltage v_T was applied across the series combination of the sample and a variable load resistor. The lock-in amplifier was used in the differential mode measuring the difference of the input terminal voltages, $v_A - v_B$. The reference voltage was applied across the B input while the sample voltage served as the A input. The resulting total input to the lock-in was the voltage v_R across the load resistor. By recording the 0° or in phase signal voltage v_0, the 90° signal voltage v_{90}, and the total reference voltage v_T, the parallel capacitance and parallel resistance of the sample were determined at each frequency. The reference voltage was measured by using the lock-in in its ac voltmeter mode.
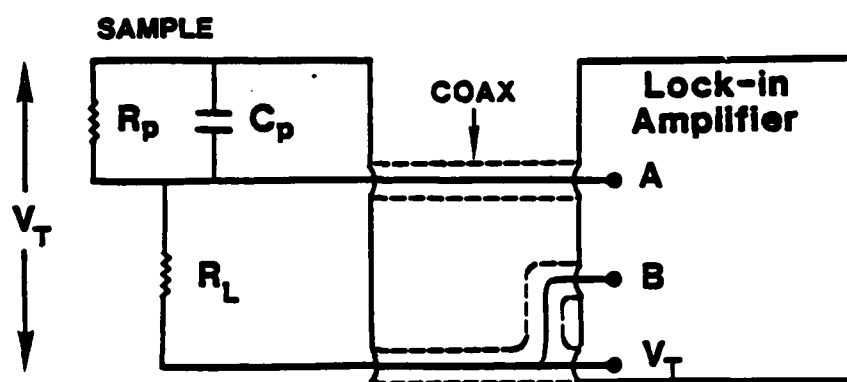
Figure 18 Variable frequency capacitance
            apparatus.

The derivation of the equations used to determine the capacitance and resistance of the sample is somewhat lengthy, so here an outline of the derivation is given. To determine the voltage drop across the load resistor, one can use voltage division to obtain,

$$v_R = \frac{R_L \, v_T}{R_L + [1/R_p + j\omega C_p]^{-1}} \, . \tag{2.15}$$

For simplicity, let $R_p = R$ and $C_p = C$. Multiplying numerator and denominator by the appropriate terms gives,

$$v_R = \frac{[R_L/R + R_L^2/R^2 + \omega^2 R_L^2 C^2 + j\omega R_L C] \, v_T}{(1 + R_L/R)^2 + \omega^2 R_L^2 C^2} \, . \tag{2.16}$$

The $0°$ or in phase voltage is then;

$$v_o = \frac{(R_L/R + R_L^2/R^2 + \omega^2 R_L^2 C^2) v_T}{(1 + R_L/R)^2 + \omega^2 R_L^2 C^2} . \tag{2.17}$$

The $90°$ voltage is,

$$v_{90} = \frac{(\omega R_L C) v_T}{(1 + R_L/R)^2 + \omega^2 R_L^2 C^2} \, . \tag{2.18}$$

From equation (2.17),

$$C = \left[\frac{(1 + R_L/R) \left[v_T(R_L/R) - v_o(R/R_L + 1) \right]}{\omega^2 R_L^2 (v_o - v_T)} \right]^{\frac{1}{2}} . \tag{2.19}$$

From equation (2.18),

$$(\omega^2 R_L^2 v_{90}) C^2 - (\omega R_L v_T) C + v_{90}(1 + R_L/R)^2 = 0. \qquad (2.20)$$

Using equations (2.19) and (2.20) to eliminate C and determine the unknown parallel resistance R we obtain,

$$R/R_L + 1 = \frac{v_T(v_T - v_o)}{v_{90}^2 + (v_T - v_o)^2}. \qquad (2.21)$$

Equation 2.20 can be solved to yield,

$$C = \frac{\omega R_L v_T \pm \sqrt{(\omega R_L v_T)^2 - 4(\omega^2 R_L^2 v_{90})(1 + R/R_L)^2 v_{90}}}{2\omega^2 R_L^2 v_{90}}. \qquad (2.22)$$

The appropriate sign of the square root in this expression is selected to give the most reasonable value of C at each frequency.

The reference voltage was set at 15 mV rms. The load resistor was varied from a few hundred ohms to about 50 kΩ. Lower values of R_L yielded flatter and probably more accurate frequency spectra for the capacitance. Regardless of the size of R_L, there was a tendency for the capacitance of the device to rise at low frequencies above its plateau value of about 600 pF. At high frequencies the measured capacitance dropped. The measured resistance tended to remain steady at lower frequencies and then rapidly drop at high frequencies.

It appears that most of the observed capacitance and resistance changes of these devices were due to in-accuracies in the measurement procedure. This conclusion was reached primarily by measuring the capacitance and resistance of a known RC circuit as a function of frequency. The values for the RC circuit were chosen at the 1 kHz RC values of the sample and so the circuit was called the mock sample. The mock sample showed much of the same trends as a function of frequency as the real device. One possible source of error which might lead to these results is error in the phase-shifting circuitry of the lock-in. This error is indicated in the lock-in manual as being worst at very low and very high frequencies. Without accounting for this error, the capacitance and resistance could at best be measured accurately only between 50 Hz and 5 kHz.

The change in capacitance and resistance of these devices upon illumination was determined using the lock-in from 20 Hz to 100 kHz. At each frequency, the capacitance changes of the sample were determined when illuminated with the two peak absorption wavelengths $\lambda = 0.86\,\mu m$ and $\lambda = 0.91\,\mu m$. Since the lock-in amplifier can filter out dc current, a blocking capacitor is not needed. According to the lock-in measurements, the capacitance of the device illuminated with $\lambda = 0.86\,\mu m$ was 3% higher than the dark

capacitance over the whole frequency range. With this measurement technique, the accuracy of the absolute values of the capacitance at each frequency is probably lower than that of the change in capacitance with illumination. Still there must be other problems with the measurement technique since, when these samples were illuminated under the same conditions and measured with the HP meter, a 10% increase in capacitance was observed.

Two improvements in the capacitance measurement using a lock-in amplifier can be made. Firstly, the ac voltage across the sample should be kept at the same value for the whole frequency range. This would entail adjusting the series load resistor or reference voltage at each frequency. Secondly, since error in the phase determination of even $0.1°$ can cause great inaccuracies in the measured capacitance, some technique for assuring proper measurement of the phase is needed. A method which may be applicable here is one which was used to measure the forward-biased capacitance of a Schottky barrier diode [19]. The problem was basically one of measuring a small capacitance in parallel with a large conductance. At very low frequencies, the in phase portion of the current swamped the out of phase current. The solution proposed was to insert a small resistor in parallel with the sample.

If considered a pure resistance, this resistor should
not affect the measured value of the device capacitance
at any frequency. The phase was adjusted until the
capacitance measured with and without the test resistor
was the same. In our case, this type of approach may
be of some use, but proper adjustment of the ac voltage
across the sample is a more critical issue.

2.2 $In_{1-x}Ga_xP/GaAs$

2.2.1 Material Properties and Device Construction

As mentioned in the introduction, it has been pre-dicted that the n(down)/p(up) configuration of the stag-gered lineup heterojunction would be the best below bandgap emitter [2]. To achieve this configuration in the $ZnSnP_2/GaAs$ system, we would need to dope the $ZnSnP_2$ n-type. Since we were unable to do this, we looked to a different materials system, $p-In_{1-x}Ga_xP/n-GaAs$. This materials system has more flexibility since both $In_{1-x}Ga_xP$ and GaAs can be made n-type or p-type. The flat band lineup of $p-In_{1-x}Ga_xP/n-GaAs$ is shown in Figure 19. The $In_{1-x}Ga_xP$ layers were grown on {111}GaAs substrates using LPE by S.Julie Hsieh [3]. $In_{1-x}Ga_xP$ is a III-V ternary alloy which can be lattice-matched to GaAs. To determine the band lineup, the necessary band parameters were ob-tained in the following manner. At each alloy composition of $In_{1-x}Ga_xP$, the energy gap was determined by its depen-dence on the lattice constant which was obtained by double-crystal x-ray diffraction scans. The lattice-matched alloy $In_{0.49}Ga_{0.51}P$ was determined in this way to have an energy gap of 1.90 eV. The energy gap of the GaAs was measured by photoconductivity on high-purity epitaxial samples to be 1.39 eV. The separation of the chemical
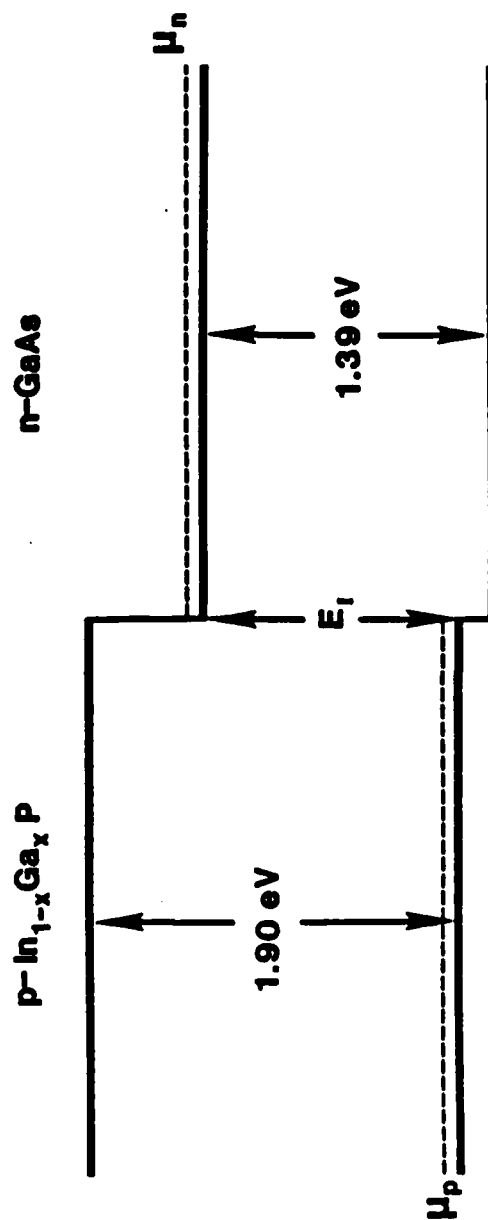
Figure 19 p-In$_{1-x}$Ga$_x$P/n-GaAs n(down)/p(up) staggered lineup.

potentials in the two materials from the closest band edge was determined by Hall measurements. The electron concentration of the GaAs substrate was found to be $n = 1.4 \times 10^{18} cm^{-3}$. Hall measurements were performed on $p-In_{1-x}Ga_xP$ layers grown on SI GaAs under the same conditions as those grown on n-GaAs. These measurements yielded a hole concentration in the $In_{1-x}Ga_xP$ of $p = 2.5 \times 10^{17} cm^{-3}$. The built-in potential V_o was determined by C-V measurements at 1 MHz.

The experimentally determined band lineup for these {111} $p-In_{1-x}Ga_xP$/n-GaAs heterojunctions is staggered, but a dielectric two-band calculation predicted the lineup to be straddling. Our experimental band offsets were $\Delta E_v = 0.08$ eV and $\Delta E_c = 0.59$ eV, which yields $E_I = 1.31$ eV. The dielectric model predicts $\Delta E_v = -0.23$ eV and $\Delta E_c = 0.28$ eV. Note that the {111} interface is not, allowing for differences in electronegativity, a charge neutral interface. We conjecture that the {111} band lineup may be shifted from the predicted straddling lineup to a staggered one due to dipoles associated with interface charge.

2.2.2 Absorption Results

Before discussing the emission mechanism and results, it is useful to briefly consider how below bandgap absorption might occur with this lineup. Figure 20 shows the $p-In_{1-x}Ga_xP$/n-GaAs heterojunction in equilibrium. Notice
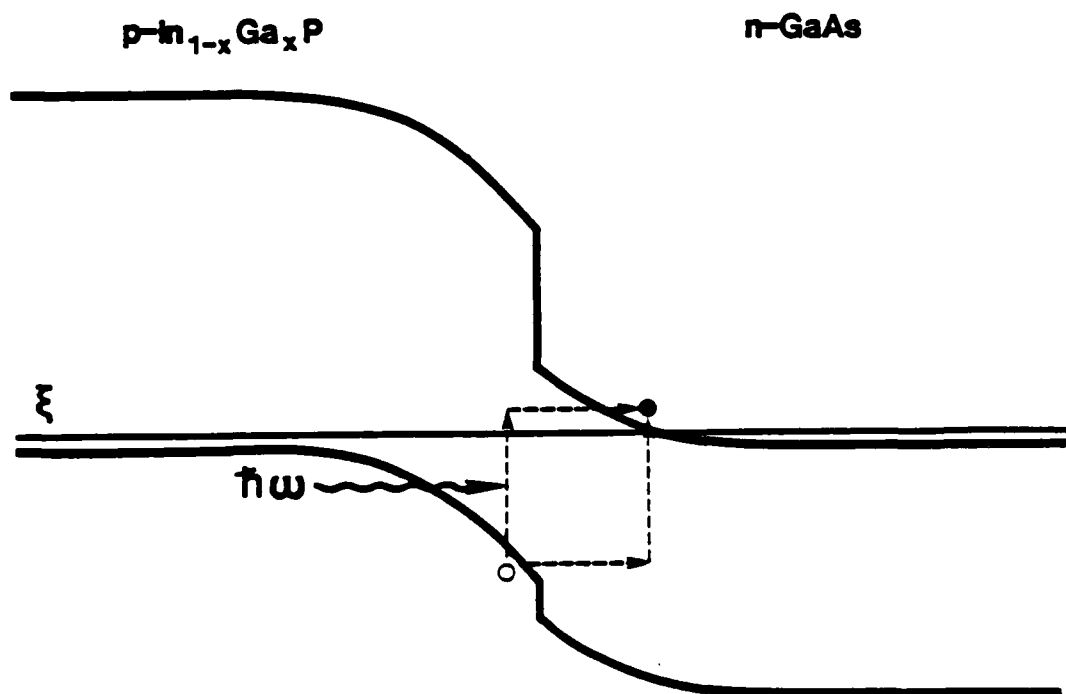
Figure 20   p-In$_{1-x}$Ga$_x$P/n-GaAs equilibrium diagram
and below bandgap absorption mechanism.

that this configuration yields an equilibrium diagram
very different from that of p-ZnSnP$_2$/n-GaAs. In the
present case there are no potential wells formed adjacent
to the interface. Even so, a possible mechanism for below
bandgap absorption still can be seen. An electron in the
valence band of In$_{1-x}$Ga$_x$P may absorb a photon and be
excited to a virtual state and then tunnel into the con-
duction band of GaAs. Another possibility would be an
electron tunneling out of the valence band of In$_{1-x}$Ga$_x$P to
a virtual state followed by photoexcitation to the GaAs
conduction band. The latter process is equivalent to hole
tunneling and so will be less probable due to the larger
hole effective mass. Room temperature absorption measure-
ments were performed on these heterostructures in the same
manner as for the ZnSnP$_2$/GaAs devices. For the In$_{1-x}$Ga$_x$P
on GaAs samples, a below bandgap peak was observed in
addition to the peaks associated with the band-to-band
absorption in the two materials. The below bandgap peak
had its half-power point at 1.31 eV. This energy cor-
responded exactly with the predicted value of E_I, however,
this exact agreement should not be taken too seriously.
The below bandgap peak increased significantly with
reverse bias. This is expected for a tunneling assisted
process since the field in the interfacial region increases
with increasing reverse bias.

2.2.3 Emission Results

To understand how this heterojunction might act as an efficient source of below bandgap emission, look at the forward bias diagram of Figure 21. Since the equilibrium lineup contained no potential wells for confinement, these must be created upon the application of sufficient forward bias. The potential wells are formed by the accumulation of majority carriers. With this n(down)/p(up) lineup, the below gap emission mechanism is essentially the same as for the p(down)/n(up) structure. The difference is that accumulated majority carriers instead of injected minority carriers are the species involved in the radiative recombination. Therefore, the emission should be stronger since there is a more plentiful supply of recombining species.

Room temperature emission experiments were performed on these (p on n) p-$In_{1-x}Ga_xP$/n-GaAs heterostructures. The samples were biased at constant current and examined with an IR viewer. All of these devices yielded little or no emission. The current typically reached 300 mA or 150 A/cm^2 before any emission was observed. When the current density reached about 250 A/cm^2, the I-V characteristics began to degrade, probably indicating heating of the device. In all cases, the emission from these devices was very much weaker than even the worst of the
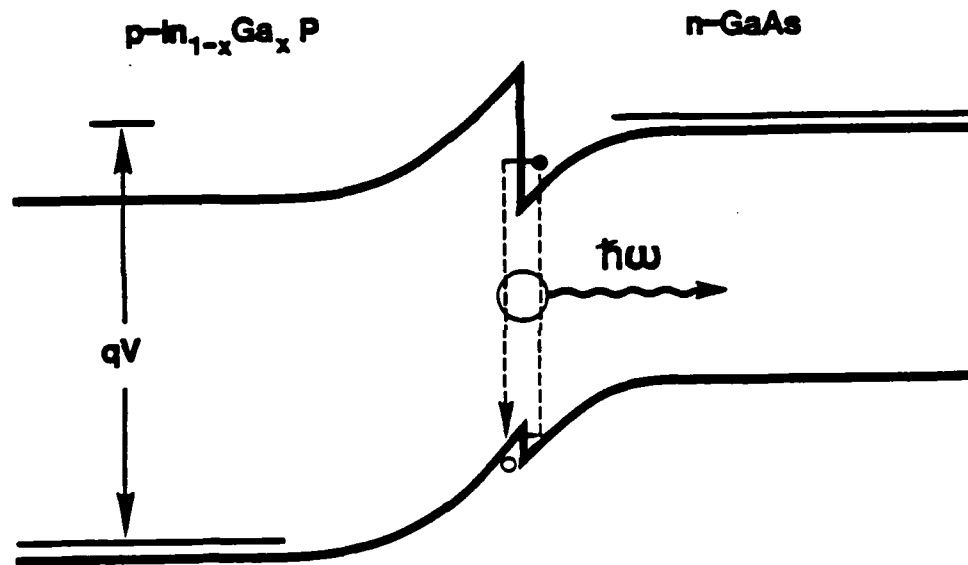
Figure 21 p-In$_{1-x}$Ga$_x$P/n-GaAs forward bias
diagram and below bandgap emission
mechanism.

$ZnSnP_2$/GaAs devices. For comparison, the forward bias emission characteristics of (n on p) $n-In_{1-x}Ga_xP/p-GaAs$ devices were also studied. Emission was observed with the IR viewer at lower current bias levels than for the p on n samples. Although the emission from the n on p samples was still smaller than that from the $ZnSnP_2$/GaAs devices, it was as good as or better than that from the p on n devices.

Our results show that for the $In_{1-x}Ga_xP/GaAs$ materials system, the n(down)/p(up) structure did not prove to be the strong below bandgap emitter as predicted. The emission was not even strong enough to obtain actual spectra through the monochromator. The emission could just barely be seen with the IR viewer. Nothing could be observed in this manner when a GaAs filter was placed in front of the sample, so we cannot even be sure that below bandgap emission was present. We believe a possible reason that this configuration did not prove to be a very good emitter is linked to the size of the band offsets. To create the potential wells of accumulated majority carriers on either side of the interface, a large forward bias must be applied. This forward bias voltage corresponds to an energy greater than either of the bandgaps. This, of course, is not possible in the case of a homojunction, because this would entail reaching and passing

the flat band condition. At flat band, for the homo-
junction, there would be no barrier to the majority
carrier diffusion and so the junction behaves like a
pure resistor. The homojunction can only be biased up to
flat band because beyond this point the heating due to
the high current would destroy the device. This of course
is the reason that the built-in potential is the maximum
voltage that can be applied safely to a homojunction. If
there are barriers to majority carrier diffusion in the
form of band offsets, this flat band condition in theory
could be reached and passed. Recall that our measured
band offsets for the $p-In_{1-x}Ga_xP$/n-GaAs devices were
ΔE_c = 0.59 eV and ΔE_v = 0.08 eV. Despite the fact that
these values may not be very accurate, the valence band
offset appears to be small. Below some critical value of
either band offset, which is related to doping and other
material parameters, prohibitively large currents will
flow in forward bias. The heterojunction in this case will
not be much different from a homojunction. Therefore,
one will not be able to go sufficiently beyond the flat
band condition to create the charge accumulation wells.
This is probably the reason our p on n devices proved
to be such poor emitters. Also the n on p emitters may
have been generally inferior to those made of $ZnSnP_2$/GaAs
since the carrier concentrations in the latter case were

much higher. The electroluminescence observed by Caine et al. [3] from the $p-Al_xIn_{1-x}As/n-InP$ devices at 1.4K indicated that these were better emitters than our n(down)/p(up) devices. The band offsets for these $p-Al_xIn_{1-x}As/n-InP$ heterojunctions were determined to be $\Delta E_c = 0.52$ eV and $\Delta E_v = 0.40$ eV . Despite the inaccuracy of band offset measurements, these values may indicate large enough barriers to current flow to allow these devices to be biased beyond the flat band condition.

2.3 C-V INTERCEPT METHOD

Theoretical models for the capacitance of an abrupt
p-n heterojunction can be made very complex. As men-
tioned earlier, the expression used to interpret the C-V
data for the $ZnSnP_2$/GaAs heterostructures neglected the
effects of interfacial charge and dipoles. That expres-
sion, equation (2.3), is valid for an abrupt heterojunction
in the depletion approximation. To modify this
model of the capacitance, let us consider an abrupt hetero-
junction with a sheet of positive charge at the interface.
For interface charge density $q\sigma\delta(0)$, Donnelly and
Milnes [18] obtain,

$$C^{-2} = \frac{2(\epsilon_p N_a + \epsilon_n N_d)(V_o - V) - q\sigma^2}{q\epsilon_n\epsilon_p A^2 N_d N_a} . \tag{4.1}$$

This is the same expression for C^{-2} as quoted earlier in
equation (2.3), except for an additional negative term in
the numerator. Equation (4.1) reveals that our previous
C-V intercept determination of V_o neglecting interface
charge will be in error if significant interface charge
is present. From (4.1) we see that $C^{-2} = 0$ when,

$$V_{o_m} = V_o - \frac{q\sigma^2}{2(\epsilon_p N_a + \epsilon_n N_d)} . \tag{4.2}$$

Here V_o is the true built-in potential whereas V_{o_m} is the

measured value. This expression reveals that regardless of the sign of any interface charge, the measured built-in potential will be smaller than the real value. For this reason, we used the largest value of V_{O_m}, presumably the most accurate value for constructing the p-ZnSnP$_2$/n-GaAs band lineup. As can be seen from (4.1), this voltage independent interfacial charge will not affect the slope of the C^{-2}-V plot and so linearity of this plot will not guarantee that interface charge is not a problem. A nonlinear C^{-2}-V plot may, however, indicate several other properties of the interface. Two interfacial effects [18] which would lead to a nonlinear C^{-2}-V plot are voltage dependent interfacial charge and dipoles.

A voltage _independent_ interfacial dipole would not affect the slope of the C^{-2}-V plot but would change the intercept and so V_{O_m}. V_{O_m} could be decreased or increased from the dipole free value depending on the sign of the dipole. A positive interfacial dipole is defined as that which serves to increase the measured value V_{O_m}. This constant dipole may vary from sample to sample. Unfortunately this dipole changes not only V_{O_m}, but also V_O and so the band offsets. For simplicity we will not concern ourselves further here with constant interfacial dipoles.

Voltage dependent interfacial dipoles and charge will contribute to a variable slope of the C^{-2}-V plot. Depending on the rate of change of the dipole and charge with voltage, the C^{-2}-V plot will curve upward or downward with increasing reverse bias. The exact details of the behavior of the C^{-2}-V plot in the presence of voltage dependent interfacial dipoles and charge will not be dealt with here, but can be found in a previous work[18]

We have been discussing the effects of interfacial charge and dipoles on the C^{-2}-V plot of an abrupt heterojunction. Now let us examine the characteristics of these plots for the $ZnSnP_2$/GaAs and $In_{1-x}Ga_xP$/GaAs devices used in our below bandgap optical measurements.

Firstly, all of the 1 MHz C^{-2}-V plots for the $ZnSnP_2$/GaAs samples studied were straight lines with nearly the same slope. The built-in potential estimates from the intercepts of these lines ranged from 1.33 to 1.75 V. As already mentioned, all V_{O_m} values except for V_{O_m}= 1.33 V confirm a staggered lineup for this heterojunction. Though I-V characteristics are not generally very precise measures of interfacial properties, for certain heterojunctions the I-V characteristics can still indicate a lower limit on V_O. The I-V curve, for the sample yielding V_{O_m}= 1.33 V, revealed a V_O at least

greater than 1.6 V. Guided by this result, let us suppose for simplicity that the variability in the V_{Om} values is due to interface charge. Assuming that $V_o = 1.75$ V, we can calculate the interface charge density necessary to shift V_{Om} to 1.33 V. If one inserts the appropriate values for the materials parameters quoted earlier into (4.2), we obtain the interface charge density, $\sigma = 1.5 \times 10^{13} cm^{-2}$.

Though several mechanisms could create an interface charge of this magnitude, let us consider the charge that would result for slight misorientations from a charge neutral orientation. Earlier, an outline of Harrison's [7] arguments concerning charge neutral heterojunction interfaces was given. The {211} orientation used for the GaAs substrate in the $ZnSnP_2$/GaAs heterojunctions was shown to be theoretically charge neutral. Using Harrison's simplified model, even slight misorientations from the charge neutral orientation would result in considerable interface charge. It can be shown that the charge density that results for small misorientations from {211} is,

$$q\sigma = (q\sqrt{3}/a^2)\sin\Theta . \tag{4.3}$$

Here a is the lattice constant and Θ is the angle of misorientation [20]. The practical limit of current routine wafer orientation techniques is roughly $\pm 0.5°$. For $0.5°$ misorientation, using $a = 5.6532$ Å for GaAs, we obtain

$\sigma = 4.7 \times 10^{12} \text{cm}^{-2}$. Since this charge is not enough to account for a measurement error in V_0 of 0.42 V, there may be other interfacial charging mechanisms involved in these devices. Next, let us consider the C^{-2}-V plots for the $In_{1-x}Ga_xP$/GaAs devices. Both lattice-matched and mismatched samples were investigated. These devices were all $\{111\}$p-$In_{1-x}Ga_xP$/n-GaAs. At 1 MHz, the C^{-2}-V plots for the lattice-matched devices were straight lines with some variability in the intercept. The mismatched samples had C^{-2}-V plots at 1 MHz which curved downwards for increasing reverse bias. These results indicate that the mismatch in these devices may create voltage-dependent interfacial dipoles and charges. The lattice mismatch in these samples was approximately 0.5% which is only slightly greater than the 0.44% mismatch associated with the $ZnSnP_2$/GaAs devices. The $\{111\}$ interface of these $In_{1-x}Ga_xP$/GaAs devices is not, however, theoretically charge neutral because of electronegativity differences. Therefore, the mismatch and the orientation together may serve to create more significant interface charge and dipole effects than found in the $ZnSnP_2$/GaAs devices.

Another interesting effect was seen in C^{-2}-V plots for measurements taken at 1 kHz. Initially C-V measurements were performed at 1 kHz on the $ZnSnP_2$/GaAs devices

using the HP LCR meter. These C-V data yielded a C^{-2}-V plot with a decreasing slope at increasing reverse bias, shown in Figure 22. The extrapolation of the reasonably linear portion of this plot at low bias yielded a higher value of V_{O_m} than for the same sample at 1 MHz. The problem may lie within the measurement technique and not the sample. The HP meter uses a 50mV rms test voltage. This may be too large for small signal approximations to be valid. When these same devices were measured at 1 kHz with a 15mV rms test voltage using the lock-in technique, linear C^{-2}-V plots were obtained. A typical result is shown as the solid line in Figure 22. The voltage intercept from this C^{-2}-V plot at 1 kHz yielded about the same value of V_{O_m} as for this sample at 1 MHz.

Apparent from these results is the great care needed to perform meaningful capacitance measurements on heterojunctions and also the difficulty in interpreting these results. Various types of capacitance measurements will undoubtedly continue to be developed as tools for analyzing heterojunction properties.
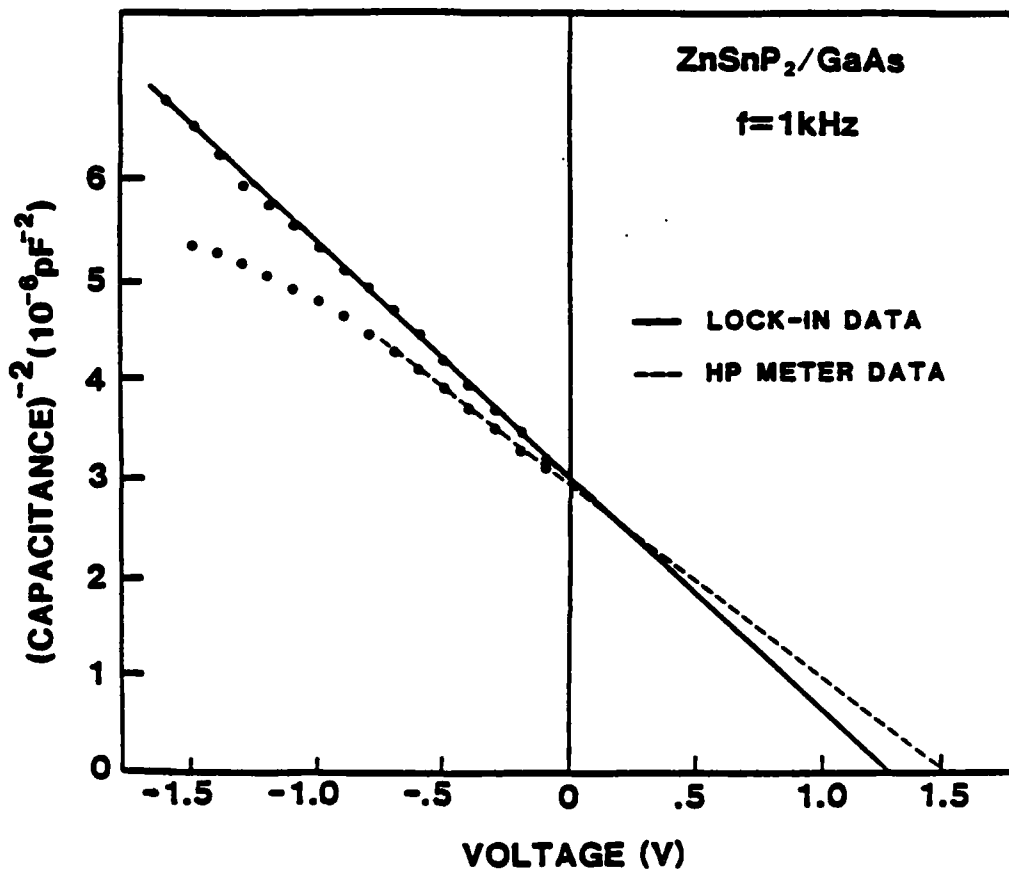
Figure 22 Comparison of C^{-2}-V for lock-in
data (15mV rms) and HP data
(50mV rms) at 1 kHz.

2.4 CONCLUSIONS

This work has sought to investigate the predicted phenomena of below bandgap emission and absorption in staggered lineup heterojunctions. These phenomena were predicted based upon a model involving mechanisms peculiar to the staggered lineup. We observed below bandgap absorption in two materials systems, $ZnSnP_2$/GaAs and $In_{1-x}Ga_xP$/GaAs and below bandgap emission in at least the first of these systems. Another research group [4] also observed below bandgap electroluminescence at low temperature in $Al_{1-x}In_xAs$/InP. Instead of reviewing these results in detail, we will discuss some of the difficulties in our interpretations of these data.

We have already discussed some of the pitfalls in the experimental determination of band offsets in heterostructures. One difficulty not previously mentioned is that of actually growing abrupt heterojunctions. Our results were all taken from samples grown by liquid phase epitaxy. There is skepticism about the ability of this growth technique to achieve sufficiently abrupt interfaces for device applications such as ours. There are other growth techniques, such as molecular beam epitaxy (MBE) and organo-metallic vapor

phase epitaxy (OMVPE), which have achieved more abrupt hetero-interfaces. We do not know how abrupt our hetero-junctions are and do not know even how critical abruptness might be to the mechanisms we have described. That is, the devices might still work if the interfaces were significantly graded, but the analysis would be much more complicated.

Another difficulty with our interpretation is the possibility that tunneling assisted transitions involving impurity or defect levels at the interface could account for our results. This alternate explanation addresses the particular problem of the shape of the below bandgap photo-response. In both the emission and absorption spectra, the below bandgap transition manifests itself in the form of a peak. One can easily account for the peak in the emission spectrum. Emission involves transitions between filled states at higher electron energies and unfilled states at lower energies. When considering the initial filled states in the conduction band well, one sees that these states are less likely to be occupied at higher energies. Also, the states in the valence band well are more likely to be filled the further down in energy one looks into the valence band. Both these effects give qualitative plausi-bility for a peak rather than a shoulder appearing in the below bandgap emission.

The below bandgap absorption peak, however, is not so easy to explain. In this case, one starts with a filled state in the valence band well and an empty state in the conduction band well. All of the obvious factors governing this type of transition; occupation numbers, density of states, and tunneling probabilities serve to increase the response at higher photon energies. There is, therefore, no obvious mechanism that would cut down the response between the minimum energy E_I and the smaller of the two bandgap energies. We would, therefore, expect to see a shoulder in the photoresponse instead of a peak.

A possible alternate explanation of our results might be tunneling assisted optical transitions involving impurity or defect levels at or near the interface. The density of states from these may peak in some region of the gap and could easily explain both the below bandgap absorption and emission peaks. We looked for evidence in our data contrary to this interpretation. We observed that the below bandgap emission and absorption peaks were coincident in energy. In principle one expects a shift between emission and absorption spectra for transitions involving impurities because of the Franck-Condon principle. As discussed earlier, this principle states that in optical transitions, electrons move so quickly that the slower

heavier lattice atoms can be considered static during the transition. The lattice relaxation tends to result in smaller energies in emission for such transitions than in absorption. Franck-Condon shifts between emission and absorption spectra for different impurity levels in various semiconductors have been measured. Unfortunately, no reliable data are available that could be directly used as a guide to estimate the shift in our case. It is possible that this shift may be too small to be observed considering the broadness of our spectral peaks. Another possible cause of the below bandgap peak in the absorption may be exciton absorption at the interface. Exciton levels can give rise to a peak in the density of states in the gap. Room temperature absorption measurements of various semiconductors have revealed below bandgap peaks due to excitonic transitions.

These are some of the problem areas in our investigation of below bandgap emission and absorption in staggered lineup heterojunctions. Although there is evidence that this type of heterojunction may prove useful through the mechanisms we have described, considerably more research into this area is needed before any solid conclusions could be reached.

2.5 REFERENCES

1. H. Kroemer, "Barrier Control and Measurements: Abrupt Semiconductors Heterojunctions", Journal of Vacuum Science and Technology, B2(3), 433 (1984).

2. H. Kroemer and G. Griffiths, "Staggered Lineup Heterojunctions as Sources of Tunable Below Gap Radiation: Operating Principle and Semiconductor Selection", IEEE Electron Device Letters, EDL-4, 20 (1983).

3. S.J. Hsieh, E.A. Patten, and C.M. Wolfe, "Below Bandgap Photoresponse of $In_{1-x}Ga_xP$/GaAs Heterojunctions", Applied Physics Letters, 45, 1125 (1984).

4. E.J. Caine, S. Subbanna, H. Kroemer, and J.L. Merz, "Staggered Lineup Heterojunctions as Sources of Tunable Below Gap Radiation: Experimental Verification", Applied Physics Letters, 45, 1123 (1984).

5. G.A. Davis and C.M. Wolfe, "Liquid Phase Epitaxial Growth of $ZnSnP_2$ on GaAs", Journal of the Electrochemical Society, 30, 1408 (1983).

6. G.A. Davis, M.W. Muller, and C.M. Wolfe, "Antiphase Domain Boundary Suppression in Chalcopyrite-on-Sphalerite Epitaxy", Journal of Crystal Growth, 69, 141-148 (1984).

7. W.A. Harrison, E.A. Kraut, J.R. Waldrop, and R.W. Grant, "Polar Heterojunction Interfaces", Physical Review B, 18, 4402 (1978).

8. C.D. Thurmond, "The Standard Thermodynamic Functions for the Formation of Electrons and Holes in Ge, Si, GaAs, and GaP", Journal of the Electrochemical Society, 122, 1133 (1975).

9. J. Franck, "Elementary Processes of Photochemical Reactions", Transactions of the Faraday Society, 21, 536 (1925).

10. E.U. Condon, "Nuclear Motions Associated with Electron Transitions in Diatomic Molecules", Physical Review, 32, 858-866 (1928).

11. A.G. Milnes and D.L. Feucht, Heterojunctions and Metal-Semiconductor Junctions. Academic Press, New York (1972).

12. H. Kroemer, "Problems in the Theory of Heterojunction Discontinuities", CRC Critical Review in Solid State Sciences, 555 (1975).

13. J.A. Van Vechten, "Quantum Dielectric Theory of Electronegativity in Covalent Systems. I. Electronic Dielectric Constant", Physical Review, 182, 891 (1969).

14. J.A. Van Vechten, "Quantum Dielectric Theory of Electronegativity in Covalent Systems. II. Ionization Potentials and Interband Transition Energies", Physical Review, 187, 1007 (1969).

15. J.L. Shay, S. Wagner, and J.C. Phillips, "Hetero-junction Band Discontinuities", Applied Physics Letters, 28, 31 (1976).

16. G.E. Stillman, C.M. Wolfe, and J.O. Dimmock, "Magnetospectroscopy of Shallow Donors in GaAs", Solid-State Communications, 7, 921-925 (1969).

17. N.A. Goryunova, M.L. Belle, L.B. Zlatkin, G.V. Loshakova, A.S. Poplavnoi, and V.A. Chaldyshev, "Optical Properties and Band Structure of $ZnSnP_2$ (Chalcopyrite and Sphalerite Modifications)", Soviet Physics-Semiconductors, 2, 1126 (1969).

18. J.P. Donnelly and A.G. Milnes, "The Capacitance of p-n Heterojunctions Including the Effects of Interface States", IEEE Transactions on Electron Devices, ED-14, 63 (1967).

19. H.L. Evans, X. Wu, and E.S. Yang, "Accurate Phase Capacitance Spectroscopy of Transition Metal Silicon Diodes", Applied Physics Letters, 46, 486 (1985).

20. H. Kroemer, "Heterostructure Devices: A Device Physicist Looks at Interfaces", Surface Science, 132, 543 (1983).

3. SPATIALLY VARYING ENERGY BANDS

With the development of special growth techniques such as molecular beam epitaxy and metal organic chemical vapour deposition, tailor-made submicron semiconductor heterostructures can now be designed. An entire new variety of structures including quantum wells, superlattices and modulation-doped structures can be conceived, and some have already led to successful device applications.

To quote a few, quantum wells are being investigated in semiconductor lasers [1] and resonant tunneling [2] for submillimeter radiation. Superlattices' potential applications include non-linear optics in relation with optical switching (bistability) [3], the Bloch oscillator [4] and the Zener oscillator [5] for submillimeter radiation. An important application of modulation doping [6] is the high electron mobility transistor, a low-noise microwave amplifier [7] and a candidate for high speed logic [8].

These semiconductor heterostructures are made of successive semiconductor crystal layers grown on top of each other. Provided the lattice parameters are closely matched, the lattices of the semiconductors essentially cohere with a minimal perturbation. Due to the special growth techniques used, the spatial variation of the semiconductor materials and/or of the doping can be controlled so as to occur in a few lattice parameters.

The study of the physical properties of these semiconductors' structures is the object of extensive theoretical and experimental effort in relation with the important potential device applications, some of which were quoted above, most of which remain however to be devised.

A fundamental property on which all these heterostructures rely is the spatial variation of the bandgap and the conduction and valence bandstructures. In this work we shall be concerned with the development of a consistent and simplified picture of spatially varying bandstructures.

Bandstructures derive from the periodic nature of the crystal potential and are therefore mathematically well-defined only for an infinite crystal. However, in practice, the concept of bands holds on a microscopic scale. This is exemplified by the use of band diagrams in classical device theory. The total classical Hamiltonian H can indeed be written as

$$H(\vec{k},\vec{r}) = E(\vec{k}) - eV(\vec{r}) \tag{1}$$

where $E(\vec{k})$ is the conduction or valence bandstructure, e the electron charge and $V(\vec{r})$ the electrostatic potential. The symbol $\vec{r}$ denotes the spatial location and $\vec{k}$ the Bloch wavevector or quasi-momentum. In a band diagram usually only the bottom of the conduction band and the top of the valence band are represented, which is equivalent to specifying $\vec{k}$.

Equation (1) together with the acceleration theorem [9] constitute the semi-classical picture on the basis of which one can describe the ballistic motion of an electron or derive (using the Boltzman Transport Equation) the standard device equations [10]. In the heterostructures discussed above, the spatial dimensions are made sufficiently small for the quantization of the electron states to be significant. One needs then to revert to the quantum mechanical form of equation (1) where the quasi-momentum is replaced by the operator

$$\vec{k} = -i \frac{\partial}{\partial \vec{r}} \tag{2}$$

and to solve the Schrödinger equation

$$i\hbar \frac{\partial}{\partial t} \psi(t,\vec{r}) = H \psi(t,\vec{r})$$

Equations (1) together with (2) are often referred to as the Wannier theorem, the derivation of which can be found in textbooks on semiconductor theory [11]. The Wannier theorem relies on two basic assumptions. The first is the one-band approximation which holds if the perturbation potential $V(\vec{r})$ is not strong enough for band-mixing to occur or interband transition such as tunneling to take place. Secondly, the perturbation potential should vary slowly or smoothly with position so as to constrain the potential overlap matrix to a diagonal representation.

These assumptions are adequate for the classical representation in which the electrons are essentially free and can be represented by a wavepacket $\Psi(\vec{r})$. For the submicron heterostructures of interest here, these assumptions do not hold, as the potential variations in modulation doped or in spatially varying bandgap structures are both large and can occur in a few lattice parameters.

In this paper we shall propose a concept of generalized bandstructures for which the Wannier theorem can be generalized and applied to submicron heterostructures.

First, we shall rederive the Wannier theorem in Section 3.1 specializing it to one-dimensional structures. Since the submicron heterostructures grown by MBE or MOCVD are layered structures, a one-dimensional picture can be implemented provided some assumptions are made. Such one-dimensional models are of heuristic interest as their simplicity promotes better insight, and they are sometimes used in semi-quantitative studies.

In Section 3.2, we discuss the extension of the Wannier theorem using the Generalized Wannier Functions and study in Section 3.3 two examples of heterostructures. These examples constitute both a test and a demonstration of applications of the generalized Wannier picture.

Finally, we present in Section 3.4 the application of the generalized
Wannier picture to "true" heterostructures and discuss the generalization of
the concept of bands to spatially varying bandstructures:

3.1 ONE-DIMENSIONAL WANNIER MODEL

In this section, we consider the problem of a crystal electron in an
external one-dimensional potential U. The total Hamiltonian of the electron
is given by:

$$H = H_0 + U(\hat{d} \cdot \vec{r})$$

where H_0 is the unperturbed crystal Hamiltonian and $U(x)$ is the
one-dimensional energy potential varying along an axis (the device axis)
represented by the unit vector $\hat{d}$.

We assume the device axis to be parallel to the lattice vector. We only
consider face-centered cubic semiconductor lattices for which a lattice vector
$\vec{R}(\vec{n})$ can be written using the orthonormal basis of the Bravais lattice as
$\vec{R}(\vec{n}) = A\vec{n}$ with $\vec{n}$ a set of integers (n_1, n_2, n_3), a* the lattic parameter
of the cubic lattice and A the matrix

$$A = \frac{a^*}{2} \begin{bmatrix} 0 & 1 & 1 \\ 1 & 0 & 1 \\ 1 & 1 & 0 \end{bmatrix}$$

We shall denote as a the modulus of the smallest lattice vector $\vec{a}$ parallel to
$\hat{d}$; a is therefore the effective lattice parameter along the direction $\hat{d}$ and
any lattice vector parallel to $\hat{d}$ is written $\vec{R} = n\vec{a}$ with n an integer.

A reciprocal lattice vector $\vec{K}$ is written in the same basis as $\vec{K}(\vec{l}) = B\vec{l}$
with l a set of integers (l_1, l_2, l_3) and B the matrix

$$B = \frac{2\pi}{a^*} \begin{bmatrix} -1 & 1 & 1 \\ 1 & -1 & 1 \\ 1 & 1 & -1 \end{bmatrix}$$

So that $AB = 2\pi$. It is easy to prove that for cubic lattices, there always exists a reciprocal lattice vector parallel to a given direct lattice vector. This is equivalent to finding the constant c such tht $\vec{K} = c\,\vec{R}$. A possible solution is $c = 8\pi/a^{*2}$, which leads to

$$\vec{1} = \begin{bmatrix} 2 & 1 & 1 \\ 1 & 2 & 1 \\ 1 & 1 & 2 \end{bmatrix} \vec{n}.$$

We shall denote q the modulus of the smallest reciprocal lattice vector $\vec{q}$ parallel to $\hat{d}$ so that any reciprocal vector parallel to $\hat{d}$ can be written $\vec{K} = \vec{1}q$ with 1 an integer. Since the lattice vector and the reciprocal lattice vector satisfy the relation

$$\vec{R}(\vec{n}) \cdot \vec{K}(\vec{1}) = 2\pi\,\vec{n} \cdot \vec{1}$$

We have that $\vec{q}$ and $\vec{a}$ satisfy

$$\vec{a} \cdot \vec{q} = aq = 2\pi p$$

with p an integer. For the <100> direction ($\vec{R} = a(1,0,0)$) we have $\vec{n} = (-1,1,1)$ and the smallest reciprocal vector is given by $\vec{1} = (0,1,1)$, so that $a=a^*$ and $p=2$.

In the extended zone scheme the Bloch function solution $\phi(\vec{k},\vec{r})$ of

$$H_0\,\phi(\vec{k}) = E(\vec{k})\,\phi(\vec{k}) \tag{3}$$

is a periodic function of $\vec{k}$ along the device direction $\hat{d}$. We can introduce a one-dimensional quasi momentum $\vec{k}$ along the device direction $\hat{d}$ defined by

$$\vec{k}(k) = \vec{k}_\perp + k\,\hat{d}$$

with $\vec{k}_\perp$ the transverse momentum perpendicular to the direction $\hat{d}$. It follows that a Bloch function along the direction $\hat{d}$ can be written as $\phi(k\hat{d} + \vec{k}_\perp, \vec{r}) = \phi(k)$ which is a periodic function of k with period q:
$\phi(k + nq) = \phi(k)$ for n an integer.

We can now define, along the direction $\hat{d}$, a one-dimensional Wannier Function $w(m,\vec{r},\vec{k}_\perp)$ as the spatial Fourier coefficient of the Bloch function $\phi(k)$

$$w(m,r,k_\perp) = 1/\sqrt{q} \int_{-q/2}^{q/2} \phi(k\hat{d} + \vec{k}_\perp, \vec{r}) \ \exp(-ikm2\pi/q)\ dk \qquad (4)$$

and reciprocally we have

$$\phi(k\hat{d} + \vec{k}_\perp, \vec{r}) = 1/\sqrt{q} \ \sum_m \ w(m,\vec{r},\vec{k}_\perp) \ \exp(ikm2\pi/q)$$

From the orthogonality property of the Bloch functions and from equation (3) one easily verifies that these Wannier functions (WF's) form an orthogonal set

$$\langle w(n)|w(m)\rangle = \int_{-\infty}^{\infty} w(n,\vec{r},\vec{k}_\perp)^* \ w(m,\vec{r},\vec{k}_\perp) \ dx' \ = \delta_{nm}$$

with $x^1 = \hat{d}\cdot\vec{r}$ and satisfy the useful relation $H_0 w(m,\vec{r},\vec{k}_1) = \sum_n E(n-m)\, w(n,\vec{r},\vec{k}_1)$
with $E(n) = 1/q \int_{-q/2}^{q/2} E(\vec{k}_1 + k\hat{d}) \exp(-ikn2\pi/q)\ dk$.

The E(n) are recognized as the Fourier coefficients of the bandstructure along the line $\vec{k}(k)$ parallel to the device axis.

For a sufficiently smooth and weak one-dimensional potential $U(\hat{d}\cdot\vec{r})$ no band mixing is expected and the transverse momentum is conserved. One can then expand the electron state in Wannier Functions of the band considered with an envelope $f(n,t)$

$$\Psi = \sum_n f(n,t) \; w(n,\vec{r},\vec{k}_\perp) \tag{5}$$

The weight function $|f(n,t)|^2$ is the probability of finding the electron at the lattice site n at time t. Replacing Ψ in the Schrödinger equation

$$H\Psi = i\hbar \frac{\partial}{\partial t} \Psi \tag{6}$$

by the expansion of equation (5), multiplying equation (6) by $w(n)^*$ and integrating over x', one obtains the Wannier recurrence equation

$$\sum_m [E(n-m) + U(n,m)] \; f(m,t) = i\hbar \frac{\partial}{\partial t} f(n,t) \tag{7}$$

where $U(n,m)$ is the matrix element given by

$$U(n,m) = \langle w(n)|U|w(m)\rangle = \int_{-\infty}^{\infty} w(n,\vec{r},\vec{k}_\perp)^* \; U(\hat{d}\cdot\vec{r}) \; w(m,\vec{r},\vec{k}_\perp) \; dx' \tag{8}$$

The one-band Wannier recurrence equation derived holds for sufficiently small perturbation potentials U. For equation (7) to be solved, both the band-structure Fourier coefficients and the matrix elements U(n,m) are required.

As expressed by equation (8) the matrix elements are evaluated from the Wannier functions. Techniques for the evaluation of the Wannier functions have been developed by Kohn [12]. The evaluation of the WF for silicon was recently reported by Evan Kane and Anne Kane [13], however, the WF derived is a linear superposition of the WF's of the four valence bands. The evaluation of realistic WF's is a complicated matter which we would like to avoid in the simple picture we intend to develop.

Some direct approximations can be derived from the properties of the WF's. In the case of simple bands it is possible to select the phase of the Bloch functions so that the WF's are exponentially localized [14]. From both the orthogonality and the tight localization of the WF's, it follows that the matrix element of a smooth potential is accurately represented by the sampling of the potential at the lattice sites

$$U(n,m) = U(x' = na/p) \, \delta_{n \, m} \tag{9}$$

We shall discuss in Section 3.3 the extent to which these approximations can be used for sharply varying potentials.

Finally, an important property of the one-dimensional WF we did not address so far is their invariance under translation from one lattice site to another. Following the approach of Wannier [15], we first write

$$\Psi(\vec{k}, \vec{r}-\vec{R}) = 1/\sqrt{q} \sum_m \exp[ikma/p] \, w(m, \vec{r}-\vec{R}, \vec{k}_\perp) \tag{10}$$

which using the translation property of the Bloch function can be written

$$\Psi(\vec{k},\vec{r}-\vec{R}) = 1/\sqrt{q} \sum_m \exp[-i\vec{k}\cdot\vec{R}] \quad \exp[ikma/p] \quad w(m,\vec{r},\vec{k}_\perp)$$

For $\vec{R} = n\vec{a}$, we have $\vec{k} \cdot \vec{R} = (k\hat{d} + \vec{k}_\perp) \cdot \vec{R} = k \hat{d} \cdot \vec{R} = kna$, and changing the index of summation we obtain

$$\Psi(\vec{k},\vec{r}-\vec{R}) = 1/\sqrt{q} \sum_m \exp[ikma/p] \, w(m+np,\vec{r},\vec{k}_\perp) \tag{11}$$

Identifying the coefficients in the series (10) and (11) we finally get

$$w(m,\vec{r}-n\vec{a},\vec{k}_\perp) = w(m+np,\vec{r},\vec{k}_\perp).$$

Considering the <100> direction for which p=2, it follows that there exist two sets of WF's each of which can be generated from two generic WF's by a lattice translation

$$w(2n,\vec{r}) = w(0,\vec{r}-n\vec{a})$$

$$w(1+2n,\vec{r}) = w(1,\vec{r}-n\vec{a})$$

The number of WF's for a given direction is therefore given by p for the face-centered cubic lattice considered. For our purpose it is convenient to picture these WF's as located at p sites along the lattice vector $\vec{a}$ associated with the direction $\hat{d}$. We can then write these WF's as

$$w(n,\vec{r},\vec{k}_\perp) = w(x'-na/p,\vec{r}_\perp,\vec{k}_\perp) = w(x'-na/p) = w(n)$$

where a is the effective lattice parameter for the direction $\hat{d}$. The one-dimensional WF we have introduced is in fact a hybrid entity, since it

corresponds to the Bloch State $k_\perp$ for the transverse coordinates $\vec{r}_\perp$. The properties of the WF's of one-dimensional lattices cannot be assumed to apply directly to the one-dimensional WF we have defined. Therefore, problems concerning the reality of the WF and the simultaneous convergence of the WF's remain to be addressed. These studies are not trivial matters for three dimensional crystals [14], in particular for lattices without a center of inversion.

In our simplified treatment we shall assume the picture developed to be truly one-dimensional. The reality and exponential localization of the WF's in one-dimensional structures are discussed by Kohn [16]. More recent work by Zak [17] raises the one-dimensional Wannier picture to the status of a well-defined representation in quantum mechanics and introduces the canonical Wannier function with minimal position uncertainty located in the zero cell of the Bravais lattice.

Zak also demonstrates that the position operator has a discrete spectrum. This implies that the applied potentials are transformed by the one-band approximation into step-like potentials. This is due to the inability of the one-band approximation to deal with the perturbation of the inner crystal potential. However, as we shall see in the next section, most of the band mixing can be formally accounted for, with the use of the generalized Wannier function. For stronger potentials it is further necessary to account for the polarization of the semiconductor [18].

END
12-85
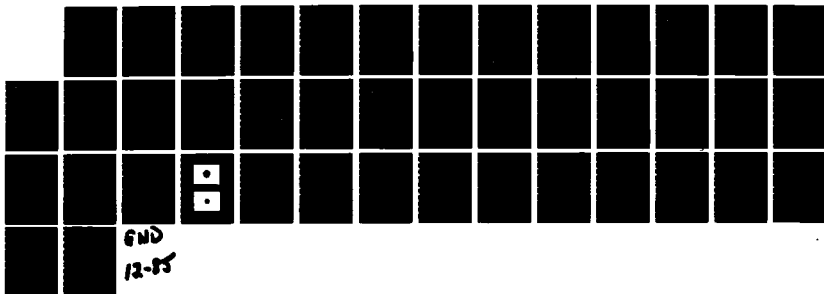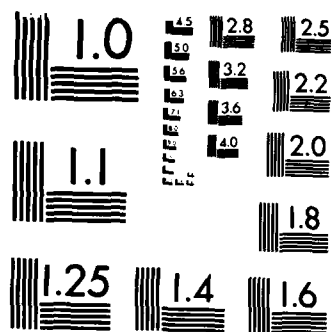
MICROCOPY RESOLUTION TEST CHART

NATIONAL BUREAU OF STANDARDS-1963-A

3.2 GENERAL WANNIER MODEL

In this section we shall be concerned only with abrupt modulation-doped heterostructures or models of abrupt heterostructures for which the bandgap is spatially varying while the bandstructure is assumed to be conserved.

The one-dimensional Wannier picture developed in the previous section is capable of handling fast spatial variation of the potential since the non-diagonal term of the matrix potential $V(n,m)$ can be accounted for. However, the formalism developed relies on the one-band approximation which strictly holds only for small potential perturbations. Its use for submicron hetero-structures seems unjustifiable. Indeed, the band-edge variation in these structures is large and band mixing is expected.

One should then resort to a multiband expansion, and the envelope equation (7) now reads

$$i\hbar \frac{\partial}{\partial t} f(n,b) = \sum_m \{E(n-m,b) f(m,b) + \sum_{b'} \langle w(n,b)|U(x)|w(m,b')\rangle f(m,b')\}$$

where b is the band index.

It is, however, possible to avoid a multiband expansion if one introduces the concept of generalized bands. As was remarked by Zak [17], "a band is a surprisingly stable entity under external perturbations." This might seem to be a paradoxical statement coming from Zak, who has been very critical of the use of the one-band approximation in general [19], and in particular for the Stark effect [20]. In fact, the existence of bands under external perturbations does not rely on the one-band approximations. A band of energy is essentially a quasi-continuum of energy states. Such an entity seems to survive numerous mistreatments such as high impurity concentrations, alloying with random distribution of two atoms on a given sublattice in III-V compounds

and even abrupt heterojunctions. However, surface-states or band tailing or even alloy and roughness scattering effects occur, and it might be more accurate to refer to these bands as generalized bands. Such bands in most cases can only be represented mathematically as resulting from the mixing of the bands of the unperturbed crystals. This is similar to the expansion of the pseudo-wavefunction in terms of plane waves in the calculation of band-structures using the pseudo-potential method; the bands evaluated result from the mixing of the bands of the empty lattice.

A one-band formalism can then be developed if one uses the exact Wannier functions instead of the Wannier functions of the unperturbed lattice. It remains to be demonstrated that such Wannier functions exist. The Wannier functions as we introduced them (see equation (4)) are defined as Fourier coefficients of the Bloch functions which are periodic in k-space. The quasi-momentum is defined by the translation operator [15] only for periodic potentials. At a heterojunction, the periodicity is broken and no quasi-momentum, Bloch functions or Wannier functions can be defined. But one can attempt to generalize the entities, as the periodicity is essentially broken only at the junction. The most obvious approach is to generalize the Wannier functions which are strongly localized on each lattice site and therefore will be strongly perturbed only at the junction itself.

The existence of generalized Wannier functions (GWF) has been theoretically established by Kohn and Onffroy [21] for one-dimensional structures. These Wannier functions can be labeled by their generalized band index; they account however for the presence of interface states in the forbidden band gap [22]. We shall denote these generalized Wannier functions $a(n,x)$. They span the same function space as the eigenfunctions of the perturbed lattice for the same generalized band.

The index n will be taken here as the site index, although depending on the potential well there may be more than one or even no GWF's associated with the interface sites. The GWF's are localized about the lattice site (or the periodic potential minima). Rehr and Kohn have shown [23] that they can be exponentially localized. An essential property of the GWF's is that they form an orthonormal set

$$\langle a(n)|a(m)\rangle = \int_{-\infty}^{\infty} a(n,x)\, a(m,x)\, dx = \delta_{n\,m}$$

The eigenfunctions are linear combinations of $a(n,x)$

$$\Psi(x,E) = \sum_{n} f(n,E)\, a(n,x)$$

with $f(n,E)$ the solution of

$$E\, f(n,E) = \sum_{m} H(n,m)\, f(m,E) \tag{12}$$

where $H(n,m)$ is the Hamiltonian matrix element given by

$$H(n,m) = \langle a(n)|H|a(m)\rangle.$$

Here H is the total Hamiltonian of the heterojunction given by

$$H = H_0 + U(x)$$

with H_0 the unperturbed crystal potential and $U(x)$ the heterojunction effective potential.

Equation (12) is similar to equation (7) except that we use the GWF instead of the unperturbed Wannier functions. The knowledge of the GWF weight $f(n,E)$ is sufficient in most applications and equation (12) can be solved if the matrix element $H(n,m)$ is known.

The derivation of the matrix element is the critical part of this method. One approach consists of first deriving the GWF's at each site. An important property of the GWF's demonstrated by Kohn and Onffroy states that for lattice sites far from the interface the GWF's approach the unperturbed WF exponentially in n,

$$a(n,x) \approx w(x-na) \quad \text{for} \quad |n| \gg 0$$

assuming the interface at n=0. Only a few GWF's are found to be perturbed or to differ from the WF as was reported by Gay and Smith [22]. It follows that a few lattice parameters away from the interface the Wannier picture developed. in Section 3.1 holds and the only remaining unknown terms are the interface Hamiltonian matrix terms.

A variational method for the derivation of the GWF has been proposed by Kohn and Onffroy for one-dimensional potentials and was tested by [22]. A three-dimensional treatment is required for the heterostructures of interest here. The derivation of the Wannier functions in three dimensions being quite involved [13], the derivation of the more complicated GWF will not be considered as a practical approach.

For our present purposes, we shall use for the Hamiltonian matrix simple approximations derived from the general properties of the Wannier Functions discussed in Sections 3.1 and 3.2.

The essential result brought out by the GWF formalism is that as long as a generalized band of energy can be assumed, it is possible to lump all the bandmixing effects into the interface Hamiltonian matrix elements, whereas the wavefunction f(n) remains given by an equivalent Hamiltonian recurrence equation.

3.3 SIMPLE EXAMPLES

We shall now consider two simple applications of the Wannier picture. The first consists of the evaluation of the resonant states in a square quantum well .5 eV deep using GaAs bandstructure. One expects to observe the interaction of the upper valley and central valley states of GaAs for such a deep well [24].

These bandstructure data, kindly furnished by Professor Karl Hess of the University of Illinois, were given at a set of sampled points in the Brillouin zone. Using the sampling theorem we reconstituted the bandstructure. The bandstructure was in addition fitted at Γ to .068 m_0. This consequently slightly altered the smoothness of the upper valley. The resulting band-structure of GaAs along Δ is shown in Figure 1. The amplitudes of the Fourier coefficients of the GaAs bandstructure along Δ are plotted in Figure 2. We present in Figure 3 the locus of the amplitude of the roots exp $[jk_i(E)a]$ that solve the equation $E(k_i) = E$ where $E(k)$ is the bandstructure along Δ. One obtains twenty roots. The roots 1 and 2 correspond to Bloch wave functions of the central valley at Γ. The roots 3 and 4 correspond to the Bloch waves of the upper valley centered on X. The unexpected behavior at X of the roots 5, 6, 7 and 8 is due to the fact that the upper valley minimum does not occur exactly at X. The shift of the X minimum is an artifact of the spectrum truncation. Since the bandstructure is slightly distorted, we do not expect these roots to contribute much. There are finally twelve remaining roots with a very high damping rate. These roots contribute only within the matching area. One observes in Figure 3 the evanescent Bloch waves being transformed into propagating Bloch waves at Γ(0 eV) and X (.3 eV).

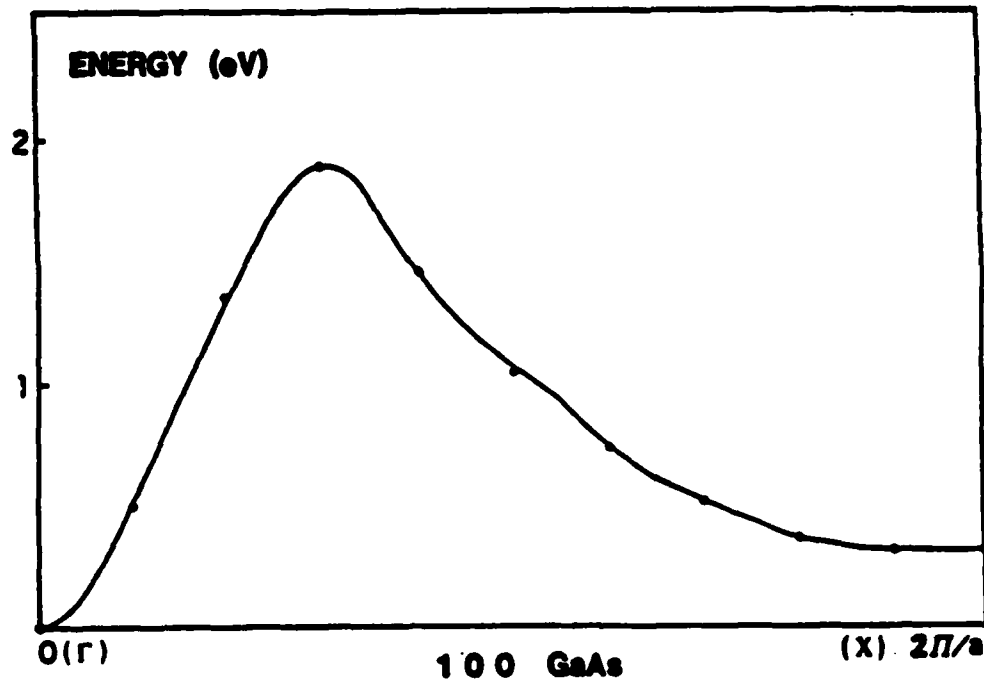FIGURE 1   GaAs bandstructure along Δ (dots: original sampled
            data); (full line: reconstructed bandstructure
            with effective mass fitted at Γ to .068 m).
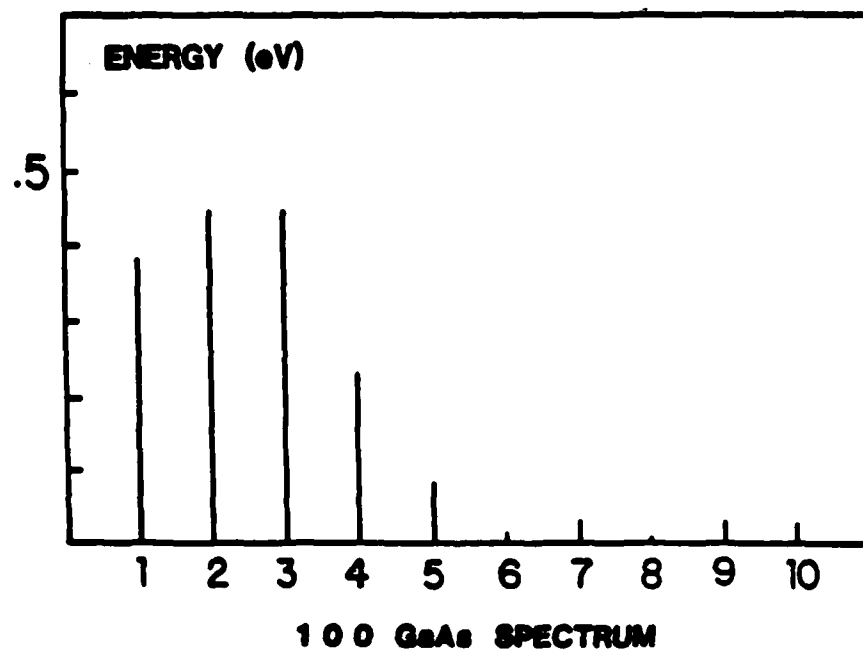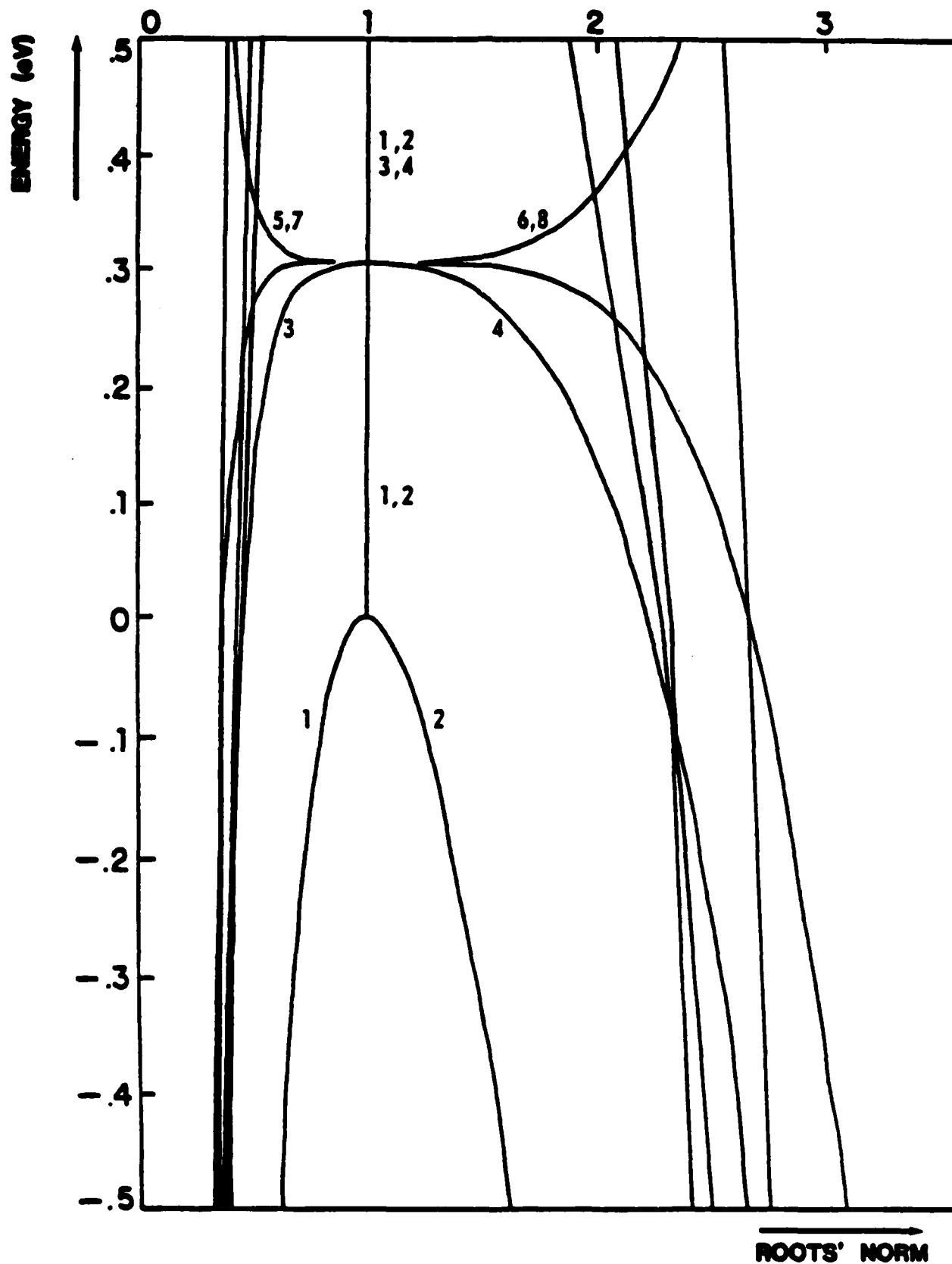

FIGURE 2   Fourier coefficients of the Γ to X bandstructure
            of Figure 1.

GaAs ROOTS' LOCUS

FIGURE 3 Locus of the roots of GaAs bandstructure $|exp(jk_i(E)a)|$ of Figure 1 as a function of the energy.

The Wannier picture calls for the matrix element of the quantum well potential. For trial purposes we evaluated numerically (with the Gauss Legendre integration technique) its matrix element using the WF's the weakly localized WF's of the empty lattice

$$w(x-ma/p) = (\frac{p}{a})^{1/2} \frac{\sin [(px/a-m)\pi]}{[(px/a - m)\pi]}$$

It is most enlightening to consider the diagonal terms plotted in Figure 4 (with an arbitrary energy scale). One observes that these diagonal terms approximately follow the assumed square potential even for such a narrow well. The energy difference (a few percent) is distributed in the non-diagonal terms· and contributes somewhat to the matching. Using the complete matrix element we found that sufficiently accurate results could be generated by directly reducing the matrix element to diagonal terms corresponding to the sampling of the assumed potential at the lattice sites (see Equation 9).

We have developed an algorithm to solve the eigenvalue problem and evaluated the locus of the resonant energy level of the square quantum well of depth .5 eV, as a function of the well width L. The result is plotted in Figure 5 (circles) and compared with the energy level locus (full line) of the effective mass approximation.

It should be pointed out that in our picture, the well width can only be varied by increments of a half-lattice parameter for the[100]direction.

We label the first resonant state 1. For a wide potential well, both the WF and the continuum methods yield the same results, since the resonant level lies at low energy where the effective mass is quite accurate. For a narrower well, one observes a divergence of the two energy plots as the effective mass approximation becomes inadequate at higher energy.
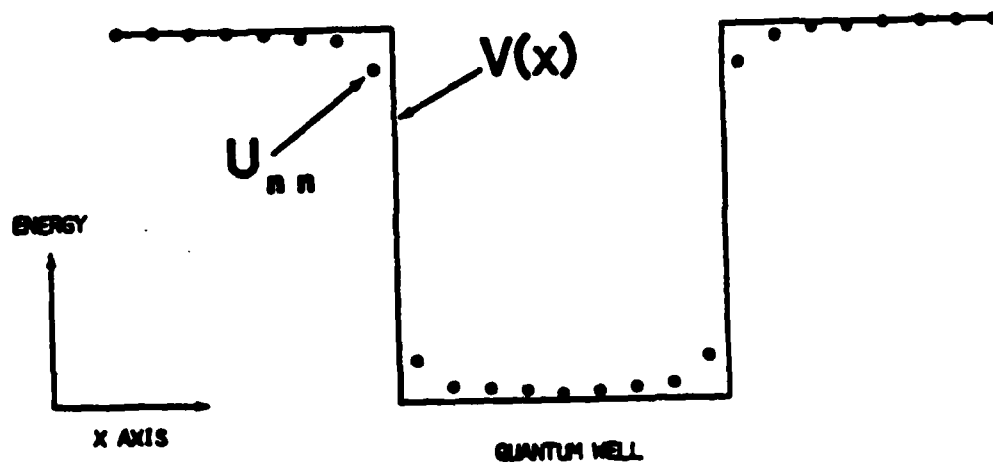
FIGURE 4   Diagonal Matrix element of a quantum well U(x),
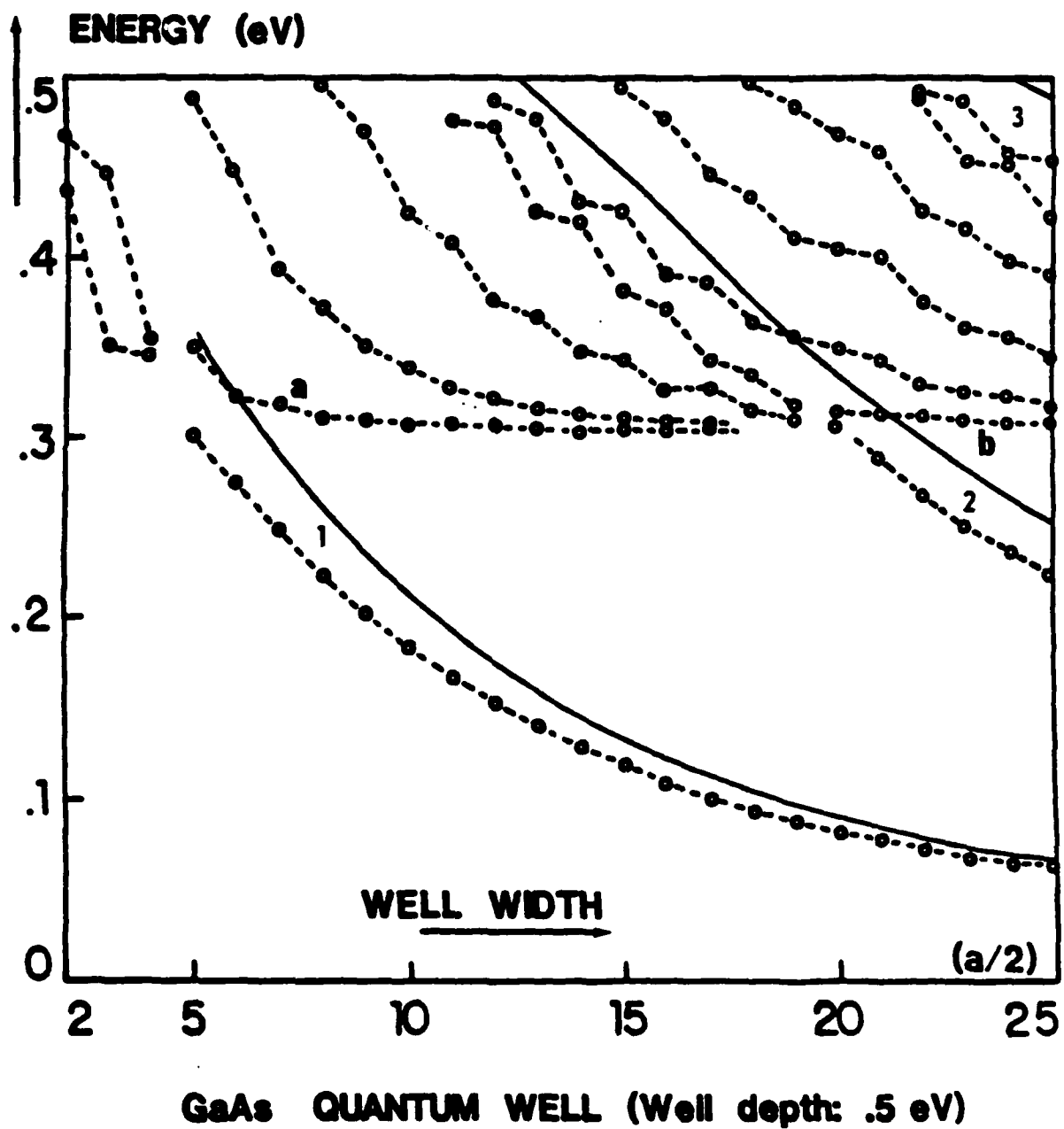   9 lattice parameters wide.

FIGURE 5   Energy levels of a GaAs quantum well, as a function
            of the well width.

For a well smaller than five lattice parameters, the first resonant state occurs above .3 eV. This resonant state results, then, from a superposition of the central valley Bloch wave and the upper valley Bloch wave. Indeed, one observes the interference of the energy locus (labeled a) of the first resonant level of the upper valley with the energy locus 1 of the central valley. This destroys the smooth variation of these energy loci as they interact. The same phenomenon occurs also as the second and third resonant level loci (denoted respectively 2 and 3) cross the X relative minimum (.3 eV). A more thorough discussion of this interference effect has been recently reported by Yia-Chung Chang and D.Z.-Y. Ting [24].

The phenomenon just described constitutes an example of what may be called a full bandstructure effect which can be handled by the generalized Wannier picture. The algorithm developed can be used to study any type of variation of the bandgap. As a second example, we consider the simple case of a superlattice made of square wells such as in the Kronig-Penney proglem [25]. We assume a simple tight-binding bandstructure $E(k) = A[1 - \cos ka]$ with the effective mass at $k=0$ selected to be .12 m_0. The well depth is .2 eV, the width and separation of the wells is chosen to be 10a so that the superlattice parameter is 20a. This leads to two resonant levels in an individual well. In Figure 6 we present the result for, successively, one, two, and twenty wells. The discrete bandstructure of the 20-well superlattice is plotted in Figure 7 (circles). This is to be compared to the bandstructure (full line) of the Kronig-Penney model in the effective mass approximation.

The low-lying bands (band 1) have a similar shape but are separated by a shift of 1 meV. This small shift originates from the use of the approximate diagonal matrix element for the superlattice potential.
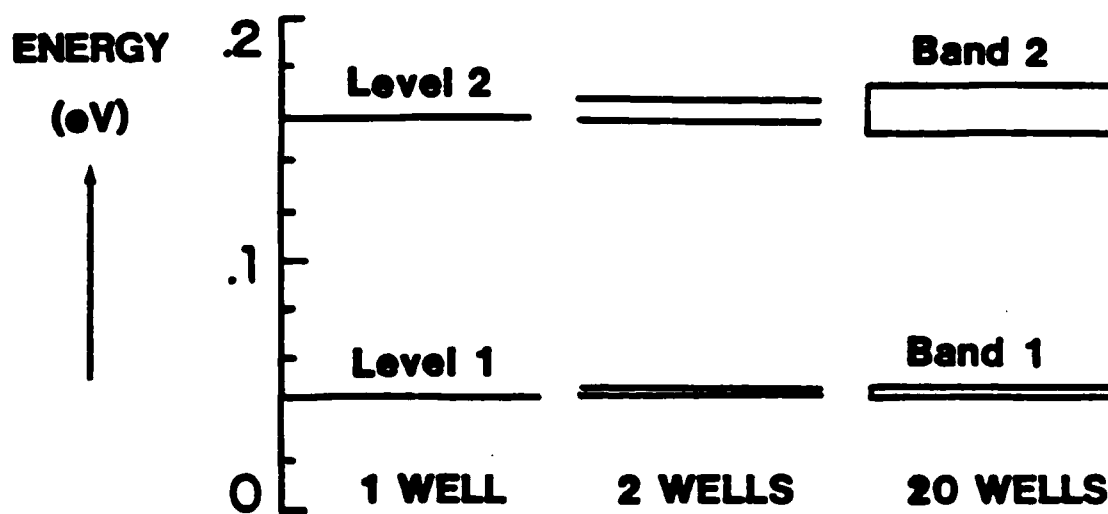
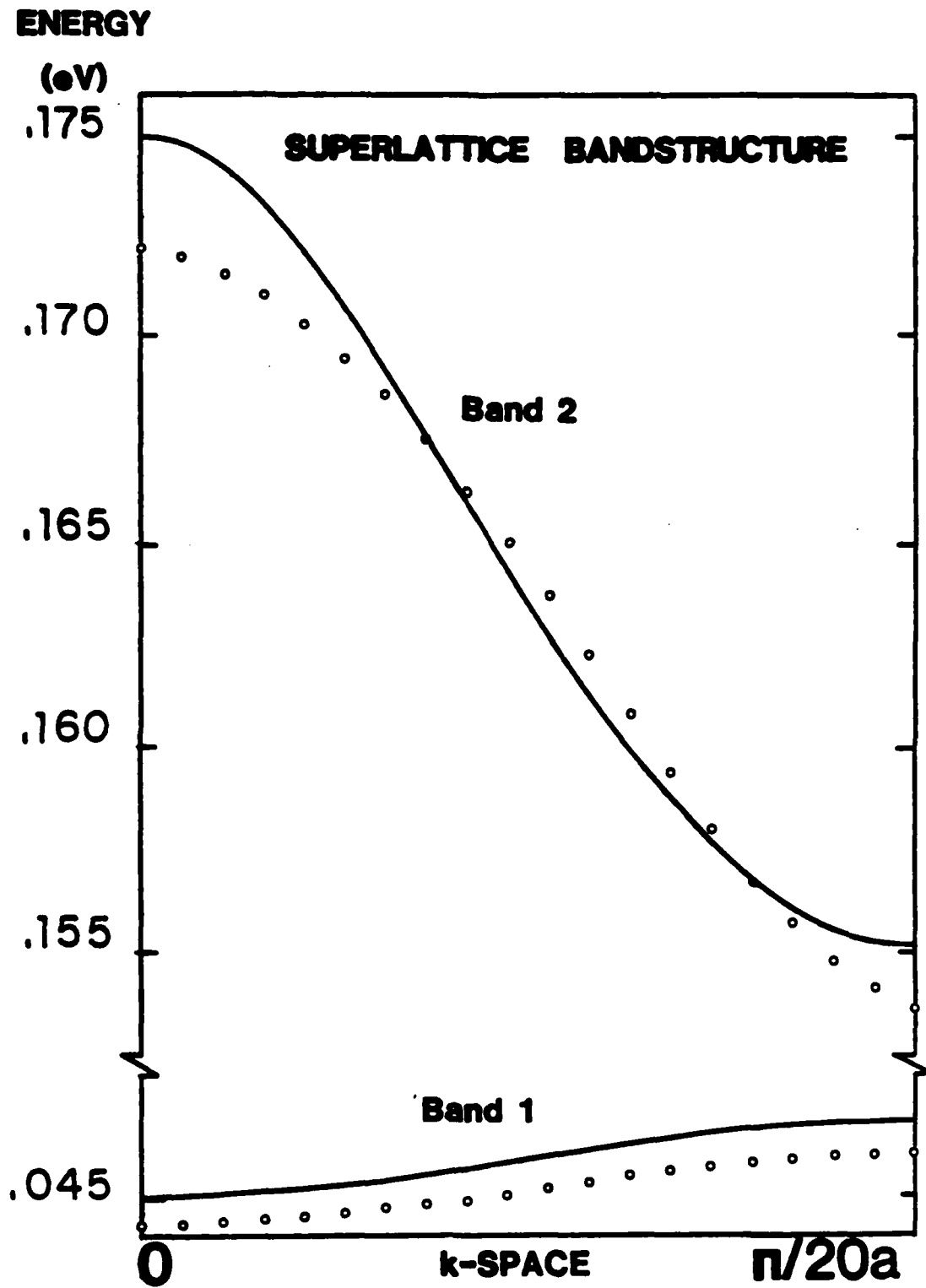FIGURE 6   Superlattice formation.

FIGURE 7   Superlattice bandstructure (o:tight binding super-
            lattice of 20 quantum wells); (full line: Kronig-
            Penney model.)

The upper bands (band 2), however, differ appreciably. Part of the difference is due to the deviation from parabolicity of the cosine band and results in a much higher conduction band maximum for the effective mass approximation. The remaining difference is essentially due to the finite character of the superlattice composed of only twenty wells.

More sophisticated structures can be studied with the algorithm developed, but this was not our purpose, as we intended to test the generalized Wannier picture using simple examples for which closed-form solutions are available.

3.4 "TRUE" HETEROSTRUCTURES

The Wannier picture developed above and its generalization does not apply so far to bandstructures varying with space. Let us point out right away that the idea of spatially varying bandstructures is an ill-defined concept, which can be made more rigorous within the framework of the generalized Wannier model.

A one-dimensional approach will breakdown for the proper description of a spatially varying bandstructure, since the variation in the bandstructure occurs in the three-dimensional k-space and therefore requires a three-dimensional matching of the Wannier envelope.

We shall, however, for simplicity partially retain the one-dimensional picture by assuming the spatially varying bandstructure to be given by

$$E(\vec{k},x) = E(k,x) + \frac{\hbar^2 \, k_\perp^2}{2 \, m^*}$$

where m^* is a transverse effective mass which is not varying in space. Such

a bandstructure does not correspond to any realizable interface but constitutes a convenient model. In this model we use the one-dimensional GWF formalism to solve for the eigenstates of this structure. A set of orthogonal GWF's noted a(n,x) can be defined as in Section 3.2. These GWF's can be exponentially localized at each lattice site n. For the case of an abrupt heterojunction, the GWF's a(n,x) approach exponentially with n the WF's of semiconductors 1 and 2, for lattice sites far from the interface (at n=0). A few lattice sites away from the interface, inside semiconductor 1, a GWF closely resembles the WF of the unperturbed semiconductor 1; the orthogonality with the GWF's of semiconductor 2 across the interface essentially affects only the exponentially decaying tail of this GWF. Finally, one is again led to the generalized one band formalism of Section 3.2 with the GWF envelope given by the one-dimensional Wannier recurrence equation (7).

The derivation of the Hamiltonian matrix elements H(n,m) is again critical to the analysis. We favor a direct evaluation of these elements which remains to be devised. In its absence alternative approaches can be conceived, and we shall demonstrate such an approach for a simple system.

First consider the trial Hamiltonian

$$H(n,m) = E(n-m,n) + U(n,m)$$

where E(n-m,n) is the bandstructure Fourier coefficient which is assumed to vary in space with the lattice site n. Such a Hamiltonian which might be proposed for a smoothly spatially-varying bandstructure is not correct as the Hamiltonian is no longer hermitean:

$$H(n,m) \neq H^*(m,n).$$

This arises as a consequence of using the intrinsically ill-defined concept of spatially dependent bandstructures. The GWF formalism is capable of accounting for the breakdown of the bandstructure. The hermiticity is indeed compatible with

$$E(m-n,n) \neq E(n-m,n)$$

it follows that the related bandstructure at the lattice site n

$$E(k,n) = \sum_{l} E(l,n) \, e^{ikla}$$

is now imaginary and therefore, as it should, has lost its usual physical meaning.

For an abrupt heterojunction, the use of GWF formalism is reduced to the derivation of matching rules. Indeed away from the interface the Wannier picture of Section 3.1 holds and the only unknown terms are the interface Hamiltonian element H(n,m).

Consider the tight-binding bandstructures given by

$$E_1(k,x) = A - A \cos ka$$

$$E_2(k,x) = B - B \cos ka$$

Where the amplitude A and B are respectively related to their effective mass by

$$A = \frac{\hbar^2}{m_1 a^2} \quad \text{and} \quad B = \frac{\hbar^2}{m_2 a^2}$$

For simplicity we evaluate the matrix element H(n,m) using the unperturbed WF's on both sides of the junction. In the tight binding approximation the only remaining unknown is then the matrix element $H(i,i+1) = - C/2$ assuming the interface is located somewhere between the lattice site i and i+1. The resulting Hamiltonian is shown around the interface in Figure 8 for U(n,m)=0.

$H_{nn'}$

$-A/2$	A	$-A/2$	0	0	0	0	0
0	$-A/2$	A	$-A/2$	0	0	0	0
0	0	$-A/2$	A	$-C/2$	0	0	0
0	0	0	$-C/2$	$B-V_0$	$-B/2$	0	0
0	0	0	0	$-B/2$	$B-V_0$	$-B/2$	0
0	0	0	0	0	$-B/2$	$B-V_0$	$-B/2$

FIGURE 8   Tight-binding Hamiltonian.

The evaluation of C depends now on the particular matching theory on which we choose to rely. There has been much published recently on the matching of wavefunctions across a heterojunction. The GWF picture proposes a general method which enables us to evaluate the wavefunction in heterostructures, but calls for the knowledge of $H(n,m)$. In its absence we intend first to relate this method to other matching theories.

Popular techniques are the effective-mass matching (see [26] and the discussion by Kroemer and Qi-Gao Zhu [27]-[28]), matching developed from the $(\vec{k} \cdot \vec{p})$ Kane model by Bastard [29], White, Margues and Sham [30]-[31], and from tight-binding arguments by White, et al. [30] and Ando and Mori [32]. A review of the different methods is briefly given in White et al. [30]. We intend to give a more complete discussion of the matching problem in a forth-coming paper.

It follows from Zhu and Kroemer's work [28] that the effective-mass matching is related for small energies to the geometrical average for the "ideal" heterostructure (type I [28]) considered here

$$C = (A \cdot B)^{1/2}$$

From Bastard's work [29], we have C given by the average

$$C = (A + B)/2.$$

Both expressions actually lead to the same results when the variation of effective-mass is small across the heterojunction. In Figure 9 we compare the effective mass matching with the geometrical average matching for a quantum well. This quantum well is made of a layer of $Ga_{.47}In_{.53}As$ sandwiched between $Al_{.48}In_{.52}As$. The effective masses are respectively taken as .041 and .075 m_0 for GaInAs and AlInAs. These effective masses should be corrected for narrow wells as the non-parabolicity is no longer negligible (see Welch, Wicks and

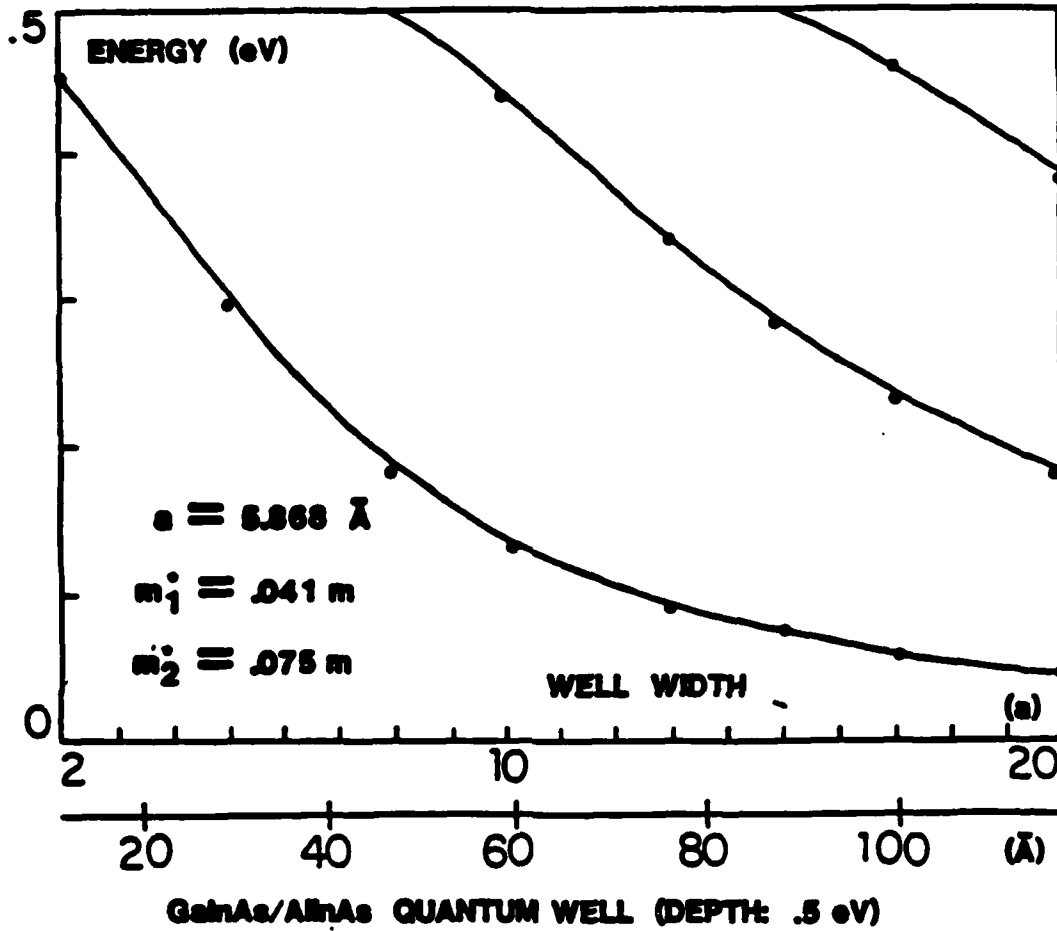FIGURE 9   Energy locus as a function of well width for
            Ga.47In.53As/Al.48In.5As quantum well (o:results
            using Wannier algorithm with the geometrical average
            matching); (full line: results using the effective
            mass matching).

Eastman [33]). The discrete energy locus is seen to agree with the continuous energy locus based on the effective mass formalism.

This result was established within the tight-binding approximation. A more refined scheme will extend the connection rules to include higher order overlaps.

3.5 CONCLUSIONS

We have introduced a generalized one-dimensional Wannier picture. This formalism enables us to handle sharp variations in potential as long as the potential strength is sufficiently moderate for the concept of a generalized band to hold. The associated band-mixing effects are then lumped into a generalized one-band Hamiltonian matrix. In the absence of knowledge of the GWF one can often rely in practice on the direct sampling of the potential at each lattice site.

The generalized one band picture applies directly to modulation-doped structures and can be used as a model of heterostructures by treating the bandgap variation as an effective potential. Another application not covered here and for which this model was in fact developed concerned the study of devices such as the Zener superlattice oscillator for which the periodicity in $\vec{k}$-space of the subband together with its spatial variation is fundamental to the device operation [5].

Finally, practical derivation of the energy levels and eigenfunctions can be performed for arbitrary potentials or heterostructure configurations using the same algorithm.

The one-dimensional generalized Wannier formalism can be used to model true heterostructures, although a rigorous treatment requires a three-dimensional GWF analysis. In the one-dimensional picture the matching

of the wavefunction across the interface is determined by the interface Hamiltonian matrix elements.

The derivation of Wannier Functions is in general a complex problem due to their orthogonality and the fact that they are not eigenfunctions of the Hamiltonian. The best procedure would be to evaluate the generalized Fourier coefficients of the generalized bandstructure directly just as the bandstructure is evaluated directly in pseudopotential calculations using variational techniques.

An alternative approach is to derive the interface Hamiltonian matrix directly from the enforcement of physical constraints. Such an approach was undertaken by Kroemer [28] and Ando and Mori [32] for maximized matching (ideal heterojunction) using current continuity. We shall report in a forthcoming paper on the extension of these matching theories to higher energy range (non-effective mass case) and for the inclusion of higher order overlap (non tight-binding cases) for both type I and II semiconductors (see [28]).

The concept of generalized bands described here is largely intuitive and has been used so far as such. The introduction of the generalized Wannier functions brings support to the concept. One interesting feature of the generalized Wannier picture is to account consistently for the concept of spatially varying bandstructure. The generalized Wannier picture appears then as an intermediate method situated between the direct study at the lattice level (e.g., LCOA techniques) and the techniques based on the effective mass approximation.

We believe that useful insights can be drawn from this ability of the GWF formalism to handle the concept of bandstructure through the use of the band-structure Fourier coefficients together with their spatial dependence on the

lattice sites. The bandstructure appears as a physical entity established in a few lattice parameters. We found that 5 to 10 lattice sites were sufficient for a close representation of a bandstructure along <100>. This is in qualitative agreement with the Wannier functions evaluated by Kane and Kane [13]. Energy bands calculated from these Wannier functions were accurate to .1 eV when the Wannier Function overlaps were evaluated to twelfth neighbors (459 individual bonds). The spatial establishment of a small effective mass requires a larger number of sites since a large number of Wannier function overlaps or bandstructure Fourier coefficients is required to fit a small effective mass while accurately reproducing the remainder of the bandstructure.

3.6 REFERENCES

[1] N. Holonyak, Jr., R.M. Kolbas, R.D. Dupuis, and P.D. Dapkus, IEEE J. Quantum Electronics QE-16, 170 (1980).

[2] T.C.L. Sollner, W.D. Goodhue, P.E. Tannenwa, C.D. Parker, "Resonant tunneling through quantum wells at frequencies up to 2.5 THz," Applied Physics Letters, Vol. 43 #3, 588 (1983).

[3] D.A.B. Miller, D.S. Chemla, D.J. Eilenber, P.W. Smith, "Large room temperature optical nonlinearity in GaAs/GaALAs multiple quantum well structures, Applied Physics Letters, Vol. 41 #8, 679 (1982).

[4] L. Esaki and R. Tsu, "Superlattice and Negative Differential Conductivity in Semiconductors," IBM Journal of Research and Development, 61 (1970).

[5] P. Roblin, "Electron States in Submicron Semiconductor Heterostructures," Dissertation, Washington University/Saint Louis, MO (1984) Chapter 3, to be published.

[6] H.L. Stormer, "Modulation doping of semiconductor superlattices and interfaces," Journal Physical Society of Japan 49, 1013 (1980).

[7] N.T. Linh, M. Laviron, P. Delescluse, P.N. Tung, D. Delagebeaudeuf, F. Diamond, and J. Chevrier, "Low-noise performance of two dimensional electron gas FET's," Proceedings 9th IEEE Cornell Biennial Conference.

[8] P.M. Solomon, "A comparison of semiconductor devices for high-speed logic," Proceedings IEEE, Vol. 70, 489 (1982).

[9] J. Callaway, "Quantum Theory of the Solid State B," New York, Academic Press (1974).

[10] J.E. Carroll, "Hot Electron Microwave Generators," American Elsevier Publishing Co., Inc., New York (1970).

[11] J.M. Ziman, "Principles of the Theory of Solids," Cambridge University Press, Cambridge (1979).

[12] W. Kohn, "Construction of Wannier Functions and Applications to Energy Bands," Physical Review B, Vol. 7 #10, 4388 (1972).

[13] E.O. Kane and A.B. Kane, "Direct calculation of Wannier Functions; Si valence bands," Physical Review B, Vol. 17 #6, 2691 (1978).

[14] J. Des Cloizeaux, "Analytical properties of n-dimensional energy bands and Wannier Functions," Physical Review 135, A698 (1964).

[15] G.H. Wannier, "Dynamics of band electrons in electric and magnetic fields," Rev. Mod. Phys. 34, 645 (1962).

[16] W. Kohn, "Analytic Properties of Bloch Waves and Wannier Functions," Physical Review, Vol 115 #4, 809 (1959).

[17] J. Zak, "Lattice representations in solids," Physical REview B, Vol. 20 #6, 2228 (1979).

[18] P. Roblin and M.W. Muller, "Coherent Zener Oscillations," Journal of Physics C, Vol. 16, 4547 (1983).

[19] J. Zak in "Solid State Physics," edited by F. Seitz, D. Turnbull and H. Ehrenreich, Academic, New York (1972).

[20] J. Avron, L. Gunther and J. Zak, "Energy uncertainty in Stark Ladders," Solid State Communications, vol. 17, 189 (1975).

[21] W. Kohn and J.R. Onffroy, "Wannier Functions in a Simple Nonperiodic System," Physical Review B, vol. 8, 2485 (1973).

[22] J.G. Gay and J.R. Smith, "Generalized Wannier Function solution to model surface potentials," Physical Review R, vol. 11, 4906 (1975).

[23] J.J. Rehr and W. Kohn, "Wannier Functions in crystal with surfaces," Physical Review B, vol. 10, 448 (1974).

[24] Yia-Chung Chang and D. Z.-Y. Ting, "Interference effect in multivalley quantum well structures," Journal of Vacuum Science Technology B 1 (2) 435 (1983).

[25] R. de L. Kronig and W.G. Penney, "Quantum Mechanics of electrons in crystal Lattices," Proceedings of the Royal Society, London vol. 130, 499 (1930).

[26] R.A. Smith, "Wave Mechanics of Crystalline Solids," John Wiley and Sons Inc., New York, Chapter 4 (1961).

[27] K. Kroemer and Qi-Gao Zhu, "On the interface connection rules for effective-mass wave functions at an abrupt heterojunction between two semiconductors with different effective mass," J. Vacuum Science Technology, vol. 21 #2, 551 (1982).

[28] Qi-Gao Zhu and Herbert Kroemer, "Interface connection rules for effective-mass wave functions at an abrupt heterojunction between two different semiconductors," Physical Review B, vol. 27 #6, 3519 (1983).

[29] G. Bastard, "Superlattice bandstructure in the envelope function approximation," Physical Review B, vol. 24, 5693 (1981).

[30] S.R. White, G.E. Margues, and L.J. Sham, "Effective-mass theory for electrons in heterostructures," Journal Vacuum Science Technology 21 (2), 544 (1982).

[31] S.R. White, and L.J. Sham, "Electronic properties of flat-band semiconductor heterostructures," Physical Review Letters, vol. 47 #12, 879 (1981).

[32] T. Ando and S. Mori, "Effective-mass theory of semiconductor heterojunctions and superlattices," Surface Science 113, 124 (1982).

[33] D.F. Welch, G.W. Wicks and L.F. Eastman, "Calculation of the conduction band discontinuity for GaInAs/AlInAs heterojunction," Journal of Applied Physics C, vol. 16, 3176 (1984).

4. LONG RANGE ORDERING

For a semiconductor alloy, $A_x B_{1-x} C$, regular solution theory indicates that the excess enthalpy or heat of mixing is given by

$$\Delta H_m = x(1-x)\Omega,$$

where Ω is an interaction parameter which contains the physics of the mixing process. For positive values of Ω we expect to have cation clustering above and phase separation below a critical temperature,

$$T_c = \frac{\Omega}{k4\ln 2} \ .$$

For negative values of Ω we expect a tendency toward cation ordering above and compound formation below T_c.

4.1 RECENT ALLOY FORMATION MODELS

There have recently been several calculations of Ω for III-V alloys based on the idea that most or all of the heat of mixing is due to bond distortion. Fedders and Muller [1] calculate Ω under the assumption that it is due to the changes in the bond lengths, a and b, of the binary compounds, AC and BC, required to form a virtual crystal lattice. This gives

$$\Omega = \lambda \ (\frac{a-b}{a+b})^2 \ ,$$

where λ can be determined from the elastic properties of the material. Mikkelsen and Boyce [2] have found from EXAFS

measurements, however, that the AC and BC bonds in alloys are within 20 percent of their values, a and b, in the binary compounds, which reduces λ by about 20.

To maintain essentially binary bond lengths, a and b, in a virtual crystal alloy the bond angles must also be distorted so that the factor of 20 reduction above is an under estimate of λ. Mikkelson [3] has taken into account both bond length and angle distortions to obtain values of Ω in good agreement with experimental values of Ω from pseudo-binary phase diagrams. Although Muller [4] has shown that bond distortion should reduce disorder below that expected for a random cation distribution of A and B, all elastic models necessarily result in a positive heat of mixing since strain energy is positive definite.

Zunger et al. [5] have included charge transfer effects with bond distortion in their model of semiconductor alloy formation. They find that, although the negative excess energy from charge transfer is small in comparison to the positive excess heat of mixing from bond distortion, the chemical charge transfer provides a means of stabilizing long range order and compound formation. This is because ordered alloys or compounds can accomodate bond distortion with less strain energy than disordered alloys with large strain energy associated with random cation distribution.

As an example, for the alloy $In_{0.5}Ga_{0.5}P$ they obtain $\Omega = +0.11eV$/atom-pair which is the same as obtained by Mikkelsen. For the compound $InGaP_2$ Zunger et al. obtain an equivalent excess energy parameter $\Omega_E = -0.047eV$/atom-pair. On this basis we can qualitatively compare alloys with In and Ga cations to those with Al and Ga cations. That is, alloys with In and Ga cations are expected to have relatively large bond distortion (atomic size differences) and large charge transfer (electro-negativity differences) compared to alloys with Al and Ga cations. Thus, the small positive or zero heat of mixing in alloys with Al and Ga cations is proportionally offset by small negative or zero excess energy due to chemical interaction.

4.2 X-RAY MEASUREMENTS

As mentioned in our last annual report [6] we have obtained some evidence for long range ordering in $In_xGa_{1-x}P$ grown on GaAs by liquid phase epitaxy. This is indicated in Figure 1 where we show back-reflection Laue photographs for (a) a {211} Ga oriented GaAs substrate and (b) an $In_{0.49}Ga_{0.51}P$ lattice-matched epitaxial layer using a Cu target. In these measurements additional spots in the photograph for the epitaxial layer could easily be interpreted as evidence for long range order. What we see instead are enhanced intensity $0\,\bar{4}\bar{6}$ and $0\,\bar{6}\bar{4}$ spots. These enhanced intensity spots were also observed in about eight other $In_xGa_{1-x}P$ layers with x between 0.49 and 0.52, but were not observed in one $Al_{0.4}Ga_{0.6}As$ layer we measured. When Laue photographs for an $In_{0.49}Ga_{0.51}P$ layer were taken with a
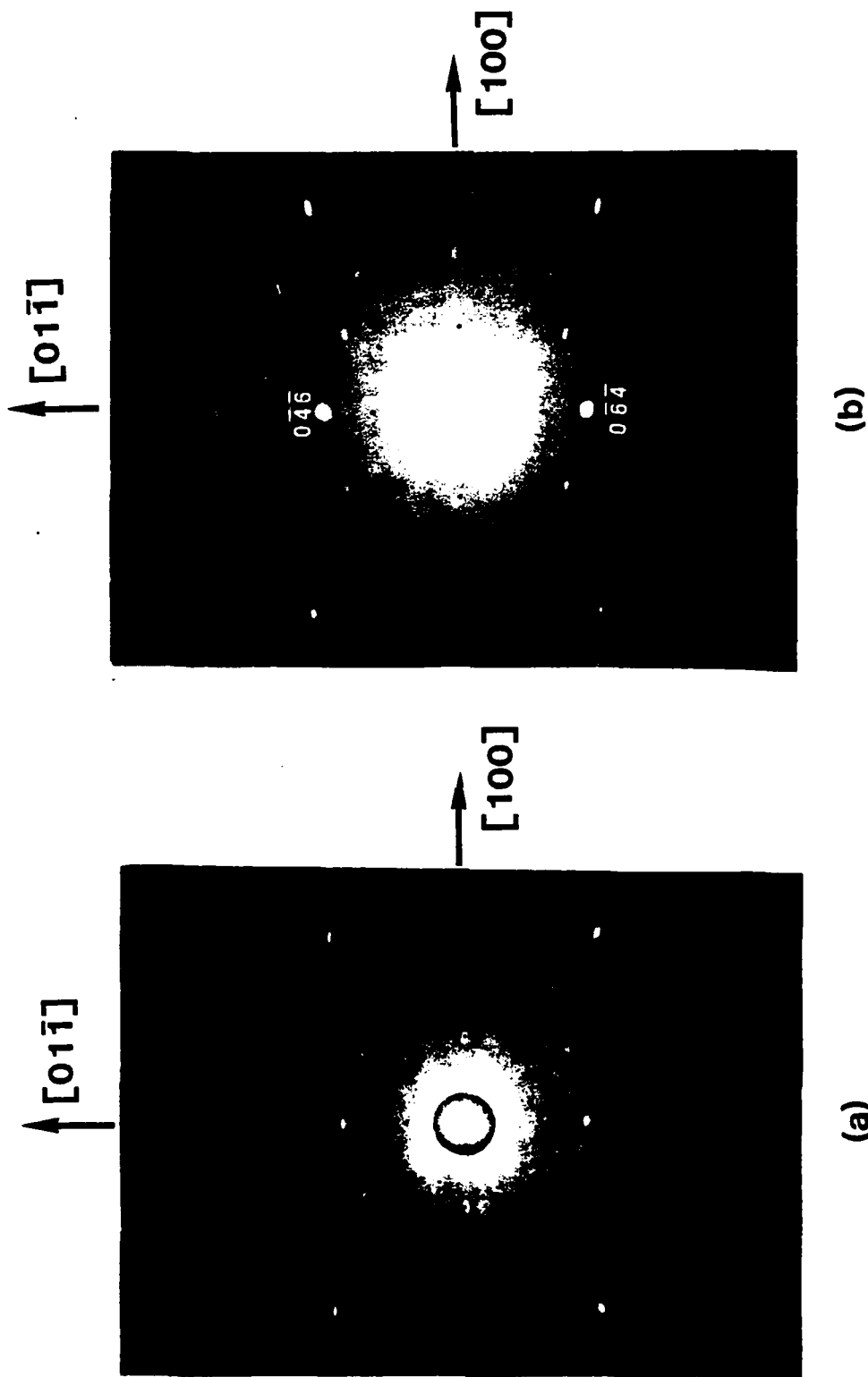
Figure 1 Back-reflection Laue photographs for (a) a {211}Ga orientated GaAs substrate and (b) an In0.49Ga0.51P lattice-matched epitaxial layer. The primary X-ray beam from a Cu target is in the [011] direction.

Mo target, the $0\bar{4}\bar{6}$ and $0\bar{6}\bar{4}$ spots were not enhanced but additional $\bar{2}\,\underline{\bar{10}}\,\underline{\bar{12}}$, $2\,\underline{\bar{10}}\,\underline{\bar{12}}$, $\bar{2}\,\underline{\bar{12}}\,\underline{\bar{10}}$, and $2\,\underline{\bar{12}}\,\underline{\bar{10}}$ were observed.

Table I. Reflections which satisfy the Bragg condition for characteristic Kα lines near the lattice constant of $In_{0.5}Ga_{0.5}P$.

Equivalent Cubic Reflection	Structure Factors			Characteristic Bragg Condition
	Sphalerite	Chalcopyrite	Layered	
032	0	0	$f_{In} - f_{Ga}$	2nd Order Cu Kα
064	$f_{In} + f_{Ga} - 2f_p$	$f_{In} + f_{Ga} - 2f_p$	$f_{In} + f_{Ga} - 2f_p$	1st Order Cu Kα
165	0	0	$f_{In} - f_{Ga}$	2nd Order Mo Kα
$2\underline{12}\,\underline{10}$	$f_{In} + f_{Ga} + 2f_p$	$f_{In} + f_{Ga} + 2f_p$	$f_{In} + f_{Ga} + 2f_p$	1st Order Mo Kα
$2\underline{12}7$	0	$f_{In} - f_{Ga}$	0	1st Order Cu Kα
$4\underline{10}9$	0	$f_{In} - f_{Ga}$	0	1st Order Cu Kα

In Table I we compare the structure factors for several reflections in the sphalerite structure and two of the most likely ordered structures for $InGaP_2$, chalcopyrite (space group $I\bar{4}2d$) and primitive layered (space group $P\bar{4}2m$) structures. First, note that superlattice structure factors are small $(f_{In} - f_{Ga})$ and will be observed only when they satisfy the

Bragg condition, $2d_{nkl} \sin \theta = n \lambda$, for one of the high intensity
characteristic x-ray lines. For example, the 2 12 7 and 4 10 9
(equivalent cubic notation) chalcopyrite reflections satisfy
the Bragg condition in 1st order for Cu Kα ($\lambda = 1.5418$Å) lines
near the lattice constant of GaAs (5.6532Å). Since we easily
observe these reflections in our chalcopyrite ZnSnP$_2$ (5.6407Å)
epitaxially grown on GaAs, we conclude that the In$_x$Ga$_{1-x}$P is
not ordering in a chalcopyrite structure.

Second, notice that the 064 set of reflections are allowed
in all three crystal structures and satisfy the Bragg condition
in 1st order for Cu Kα. If the In$_x$Ga$_{1-x}$P has a layered
structure, these 064 reflections could be enhanced by 032
reflections, which satisfy the Bragg condition in 2nd order
for Cu Kα. In a similar manner the 2 12 10 reflections, which
satisfy the Bragg condition in 1st order for Mo Kα ($\lambda = 0.7107$Å),
could be enhanced by 165 reflections, which satisfy the Bragg
condition in 2nd order for Mo Kα.

Using tabulated atomic scattering factors [7] we can
calculate the intensity of the 064 Laue spots that would
be expected with different materials and crystal structures.
Taking into account 032, 064, 096, and 0 12 8 reflections,
the following reflected intensity ratios are obtained.

$\dfrac{\text{InGaP}_2}{\text{In}_{0.5}\text{Ga}_{0.5}\text{P}}$	$\dfrac{\text{In}_{0.5}\text{Ga}_{0.5}\text{P}}{\text{GaAs}}$	$\dfrac{\text{InGaP}_2}{\text{GaAs}}$
3.5	60	220

Although this calculation neglects absorption and secondary
extinction, it shows that the 064 enhancement shown in

Figure 1 could be simply due to the difference between sphalerite $In_{0.5}Ga_{0.5}P$ and GaAs and not layered $InGaP_2$ and GaAs.

4.3 LAYERED STRUCTURE

Recently, Kuan, Kuech and co-workers[8] have reported long-range order in $Al_xGa_{1-x}As$. They claim to see the most pronounced evidence for ordering from $Al_{0.75}Ga_{0.25}As$ grown on {110}GaAs at 700°C by organo-metallic vapor phase epitaxy. Electron diffraction measurements, which are sensitive to surface structure, were used to indicate the presence of a layered crystal structure (the $P\bar{4}2m$ space group discussed above) with c-axes orientations in the growth plane. No significantly different physical properties, however, were obtained for this material. Although this report is probably premature for the reasons indicated, there is some merit to their claim.

A fairly definitive x-ray experiment which would indicate the presence of a layered crystal structure is shown schematically in Figure 2. The geometry of the experiment is the same as that used to obtain the back-reflection Laue photographs shown in Figure 1. The layered face centered cubic cation sublattice with cations as open and closed circles and [001] c-axes is shown as observed in the [$\bar{1}$00] direction. Figure 2(a) shows that for this c-axis orientation reflections from the (046) planes between the (023) planes do not cancel out (023)
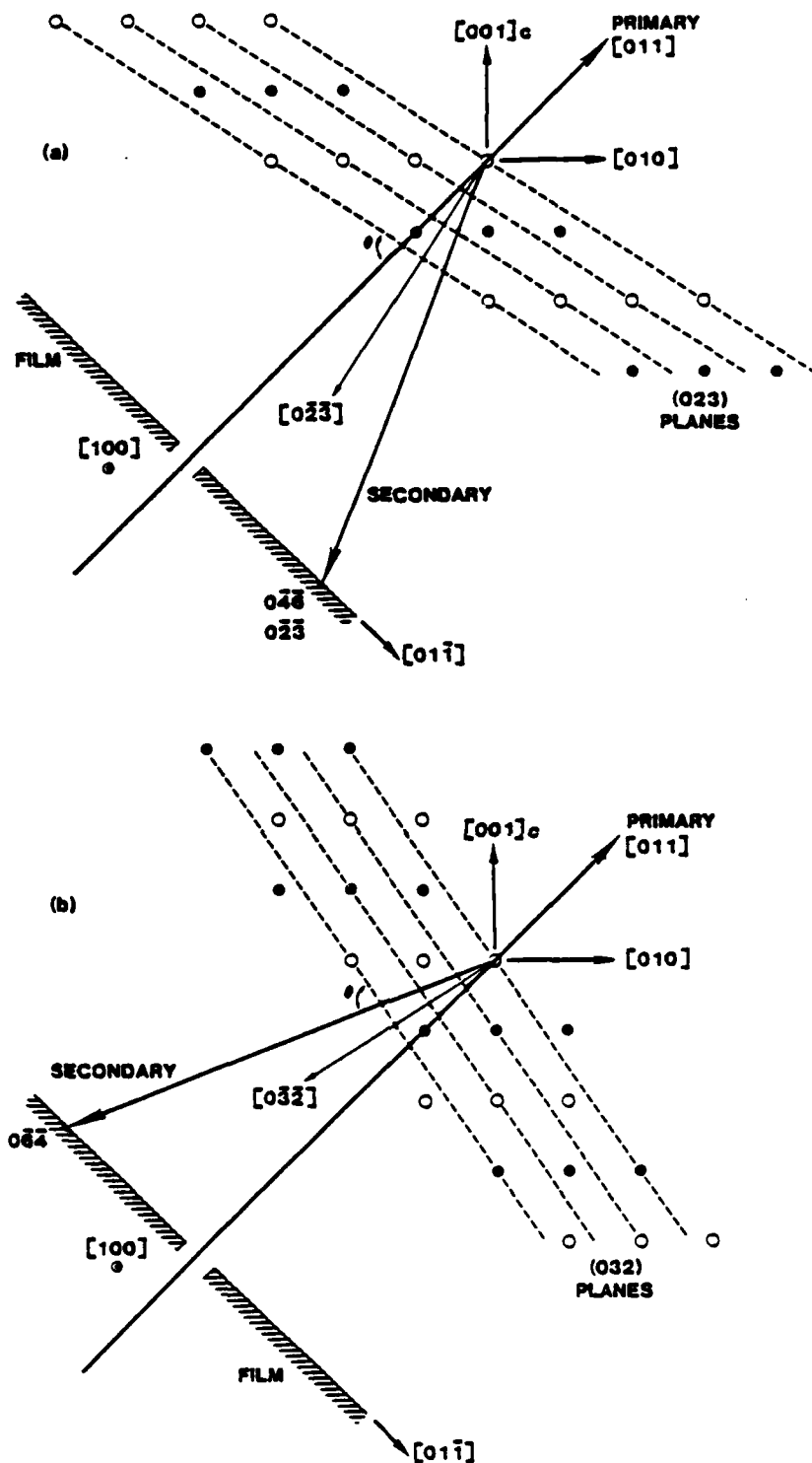
Figure 2 Schematic of a back-reflection Laue measurement
which would indicate the presence of a layered
crystal structure. The orientation of the
experiment is the same as that used to obtain
the photographs in Figure 1.

reflections. Thus, both $0\bar{4}\bar{6}$ and $0\bar{2}\bar{3}$ superimpose on the bottom of the film. Figure 2 (b) shows, however, that for the same c-axis orientation reflections from the (064) planes cancel out reflections from the (032) planes. Thus, only $0\bar{6}\bar{4}$ is observed on the top of the film. A significant difference in intensity of these spots on the film (we calculate 3.5 for In and Ga cations), therefore, would indicate a layered structure with one c-axis.

If the c-axis in Figure 2 were in the [010] direction, one can see that the $0\bar{6}\bar{4}$ and $0\bar{3}\bar{2}$ at the top of the film would superimpose while the $0\bar{2}\bar{3}$ reflection would be cancelled by $0\bar{6}\bar{4}$ at the bottom. For the c-axis in the [100] direction both $0\bar{3}\bar{2}$ and $0\bar{2}\bar{3}$ reflections would be cancelled, since the layered structure looks like a sphalerite structure to an [011] x-ray beam orthogonal to the c-axis. The examination of a tetragonal structure with fixed primary x-ray beam orientation and three c-axis orientations is equivalent to the examination of a tetragonal structure with fixed c-axis orientation and three primary x-ray beam orientations. The latter, of course, is experimentally achievable and we summarize potential observations in Table II.

Table II Summary of conclusions that can be obtained from Laue measurements with primary beam in three <110> directions.

Beam Directions	Enhanced 064 Spots		P$\bar{4}\bar{2}$m c-axes
[011]	$0\,\bar{4}\,\bar{6}$	—	
[101]	—	$\bar{4}\,0\,\bar{6}$	[001]
[110]	—	—	
[011]	$0\,\bar{4}\,\bar{6}$	$0\,\bar{6}\,\bar{4}$	[001]
[101]	—	$\bar{4}\,0\,\bar{6}$	and
[110]	$\bar{4}\,\bar{6}\,0$	—	[010]
[011]	$0\,\bar{4}\,\bar{6}$	$0\,\bar{6}\,\bar{4}$	[001]
[101]	$\bar{6}\,0\,\bar{4}$	$\bar{4}\,0\,\bar{6}$	[010] and
[110]	$\bar{6}\,\bar{4}\,0$	$4\,\bar{6}\,0$	[100]

The salient feature of the experiments indicated in Table II is that, to determine the number of c-axes in a layered sample, x-ray measurements must be taken with the primary beam in at least two of the <110> directions indicated. At the present time we have looked at our $In_xGa_{1-x}P$ samples with the primary beam in only one <110> direction. For these samples no asymmetry in 064 spot intensity has been observed which could not be attributed to slight misorientation of the primary beam.

4.4 CONCLUSIONS

From the discussion above we conclude that charge transfer effects in III-V alloys may provide a mechanism for stabilizing equilibrium long range order and compound formation. The resulting total negative excess energy involved, however, appears to be sufficiently small that low growth temperatures and kinetic effects, such as substrate orientation, may be critical factors. This appears to be the case for the recently reported ordering in $Al_xGa_{1-x}As$ and should also be true for alloys with larger atomic size and electronegativity differences.

4.5 REFERENCES

1. P.A. Fedders and M.W. Muller, J. Phys. Chem. Solids 45, 685 (1984).

2. J.C. Mikkelsen, Jr. and J.B. Boyce, Phys. Rev. Lett. 49, 1412 (1982).

3. J.C. Mikkelsen, Jr., J. Electrochem. Soc 132, 500 (1985).

4. M.W. Muller, Phys. Rev. B 30, 6196 (1984).

5. A. Zunger et al., Electronic Materials Conference, June 1985.

6. C.M. Wolfe et al., "Clustering and Ordering in III-V Alloys", Annual Scientific Report No. WU/SRL-59583A-3, 31 July 1984.

7. International Tables for X-Ray Crystallography, Vol. 3 (Kynoch Press, Birmingham, 1968).

8. T.S. Kuan et al., Phys. Rev. Lett. 54, 201 (1985); T.F. Kuech et al., Electronic Materials Conference, June 1985.

5. PERSONNEL

The personnel who worked on this grant during the current reporting period were as follows:

Prof. C.M. Wolfe, Principal Investigator

Prof. M.W. Muller, Faculty Associate

Ms. S. Julie Hsieh, Research Assistant

Ms. Elizabeth A. Patten, Research Assistant

Mr. Keith A. Salzman, Research Assistant

The students who have completed requirements for advanced degrees and/or received degrees on this grant up to the present time are:

May 1983, Gary A. Davis, Doctor of Science, "Preparation and Properties of $Zn_xCd_{1-x}SnP_2$ Epitaxially Grown on InP and GaAs";

August 1984, Patrick Roblin, Doctor of Science, "Electron States in Submicron Semiconductor Heterostructures" (partial support);

August 1985, S. Julie Hsieh, Doctor of Science, "$In_{1-x}Ga_xP$-GaAs Heterojunctions";

August 1985, Elizabeth A. Patten, Doctor of Science, "Below Bandgap Emission and Absorption in Staggered Lineup Heterojunctions".

6. PUBLICATIONS

1. G.A. Davis and C.M. Wolfe, "Liquid Phase Epitaxial Growth of $ZnSnP_2$ on GaAs", J. Electrochem. Soc. __130__, 1408 (1983).

2. G.A. Davis, M.W. Muller, and C.M. Wolfe, "Antiphase Domain Boundary Suppression in Chalcopyrite-on-Sphalerite Epitaxy", J. Crystal Growth __69__, 141 (1984).

3. P.A. Fedders and M.W. Muller, "Mixing Enthalpy and Composition Fluctuations in Ternary III-V Semiconductor Alloys", J. Phys. Chem. Solids __45__, 685 (1984).

4. M.W. Muller, "Composition Correlations in Ternary Semiconductor Alloys", Phys. Rev. __B 30__, 6196 (1984).

5. S. Julie Hsieh, Elizabeth A. Patten, and C.M. Wolfe, "Below Bandgap Photoresponse of $In_{1-x}Ga_xP$-GaAs Hetero-junctions", Appl. Phys. Letters __45__, 1125 (1984).

6. E.A. Patten, G.A. Davis, S.J. Hsieh, and C.M. Wolfe, "Below Bandgap Emission and Absorption in $ZnSnP_2$/GaAs Heterojunctions", IEEE Electron Device Letters __6__, 60 (1985).

7. P. Roblin and M.W. Muller, "On Spatially Varying Bandstructures", Phys. Rev. B (to be published).

8. E.A. Patten, S.J. Hsieh, G.A. Davis, and C.M. Wolfe, "Below Bandgap Emission and Absorption in Staggered Lineup Heterojunctions", submitted to Microscience.

7. TALKS

1. G.A. Davis, "Preparation and Properties of $Zn_xCd_{1-x}SnP_2$ Epitaxially Grown on InP and GaAs", Seminar, M.I.T. Lincoln Laboratory, Lexington, Mass., 1 April 1983.

2. —————, IBM Research, Yorktown Heights, N.Y., 4 April 1983.

3. —————, General Motors Research Laboratory, Detroit, Mich., 8 April 1983.

4. —————, Varian Associates, Palo Alto, Calif., 11 April 1983.

5. M.W. Muller, "Mixing Enthalpy and Composition Fluctuations in Ternary III-V Semiconductor Alloys", Seminar, SRI International, Menlo Park, Calif., 20 December 1983.

6. S. Julie Hsieh, "$In_{1-x}Ga_xP$-GaAs Heterostructures", Seminar, Hewlett Packard, Palo Alto, Calif., 7 November 1984.

7. —————, Texas Instruments, Dallas, Tex., 17 December 1984.

8. —————, GTE Laboratories, Waltham, Mass., 20 December 1984.

9. —————, AT&T Bell Laboratories, Murray Hill, N.J., 14 February 1985.

10. —————, Universal Energy Systems, Dayton, Ohio, 5 March 1985.

11. —————, AT&T Bell Laboratories, Murray Hill, N.J., 19 March 1985.

12. —————, RCA Laboratories, Princeton, N.J.,
20 March 1985.

13. Elizabeth A. Patten, "Below Bandgap Emission and
Absorption in Staggered Lineup Heterojunctions",
Seminar, AT&T Bell Laboratories, Murray Hill, N.J.,
1 April 1985.

14. —————, Santa Barbara Research Center, Goleta,
Calif., 9 April 1985.

15. —————, SRI International, Menlo Park, Calif.,
12 April 1985.

16. —————, TRW, El Segundo, Calif., 29 April 1985.

17. —————, M.I.T. Lincoln Laboratory, Lexington, Mass.,
6 May 1985.